Human hippocampal CA3 uses specific functional connectivity rules for efficient associative memory
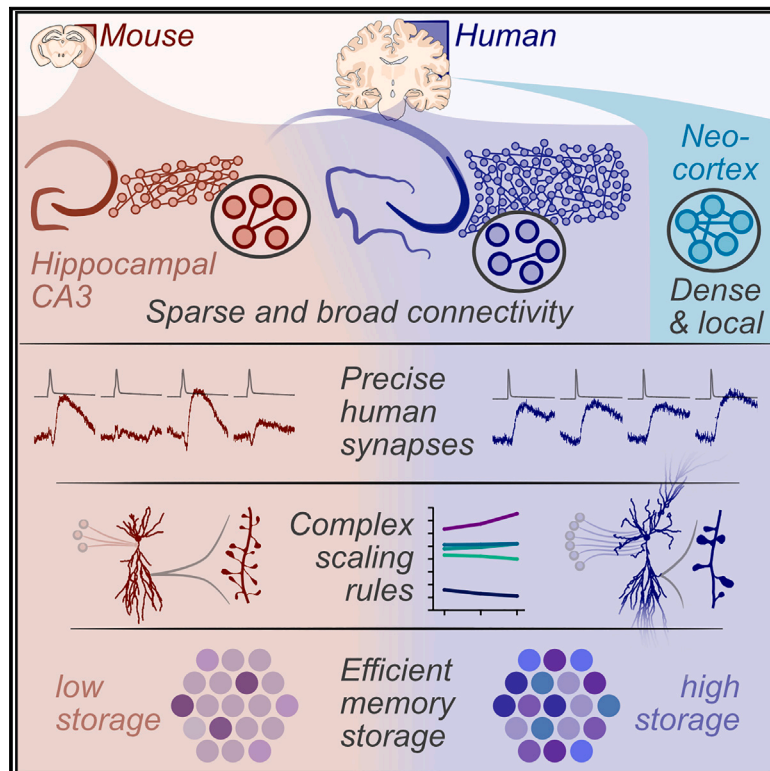
Graphical abstract

Highlights

- Human hippocampal CA3 uses sparser synaptic connectivity than neocortical circuits

- Connectivity sparsifies across species, reflecting a broad circuit architecture

- Human CA3-CA3 synapses have reliable and precise transmission

- Sparse connectivity and reliable transmission optimize memory storage capacity

Authors

Jake F. Watson, Victor Vargas-Barroso, Rebecca J. Morse-Mora, ..., Matthias Tomschik, Karl Rössler, Peter Jonas

Correspondence

jake.watson@ist.ac.at (J.F.W.),
peter.jonas@ist.ac.at (P.J.)

In brief

Human hippocampal CA3 networks use sparse and broad synaptic connectivity, and their recurrent synapses employ reliability, precision, and long integration times to enhance memory capacity. Thus, the human hippocampus is distinct from both rodent counterparts and human neocortical circuits.

CellPress

Cell

Article

Human hippocampal CA3 uses specific functional connectivity rules for efficient associative memory

Jake F. Watson,[1,*] Victor Vargas-Barroso,[1] Rebecca J. Morse-Mora,[1] Andrea Navas-Olive,[1] Mojtaba R. Tavakoli,[1] Johann G. Danzl,[1] Matthias Tomschik,[2] Karl Rössler,[2] and Peter Jonas[1,3,*]
[1]Institute of Science and Technology (ISTA), 3400 Klosterneuburg, Austria
[2]Department of Neurosurgery, Medical University of Vienna, 1090 Vienna, Austria
[3]Lead contact
*Correspondence: jake.watson@ist.ac.at (J.F.W.), peter.jonas@ist.ac.at (P.J.)
https://doi.org/10.1016/j.cell.2024.11.022

SUMMARY

Our brain has remarkable computational power, generating sophisticated behaviors, storing memories over an individual's lifetime, and producing higher cognitive functions. However, little of our neuroscience knowledge covers the human brain. Is this organ truly unique, or is it a scaled version of the extensively studied rodent brain? Combining multicellular patch-clamp recording with expansion-based superresolution microscopy and full-scale modeling, we determined the cellular and microcircuit properties of the human hippocampal CA3 region, a fundamental circuit for memory storage. In contrast to neocortical networks, human hippocampal CA3 displayed sparse connectivity, providing a circuit architecture that maximizes associational power. Human synapses showed unique reliability, high precision, and long integration times, exhibiting both species- and circuit-specific properties. Together with expanded neuronal numbers, these circuit characteristics greatly enhanced the memory storage capacity of CA3. Our results reveal distinct microcircuit properties of the human hippocampus and begin to unravel the inner workings of our most complex organ.

INTRODUCTION

We all experience the remarkable computational power of the human brain. It generates exquisite behavioral sequences, stores memories over a lifetime, and provides us with our complex cognitive functions such as imagination and consciousness. Yet how cells and circuits generate these incredible phenomena remains unknown. In particular, we do not know whether the human brain is simply a scaled version of the extensively studied rodent brain[1,2] or whether its uniqueness is produced by the specific properties of cells,[3,4] dendrites,[5–7] or synapses.[8–11] Distinguishing between these possibilities requires structural and functional analysis of living human brain tissue. However, only very few experimental studies have directly examined the properties of human circuits. This is particularly striking for the hippocampus, which is the most intensively studied region of the rodent brain, yet of its cellular function in humans, we know very little. The hippocampal CA3 region is the largest autoassociative network in the brain, with a fundamental role in memory storage.[12,13] While its cellular, synaptic, and microcircuit properties were thoroughly studied in rodents,[14,15] functional data from human CA3 are unavailable.

Currently, the only way to tackle these fundamental questions is to obtain direct recordings from living brain tissue extracted from human patients. It is generally believed that such measurements are only possible in neocortical tissue, which is thought to be unaffected by the underlying disease and better preserved during surgery.[8,16–18] However, recent work shows that hippocampal tissue extracted from patients during epilepsy surgery is heterogeneous, including patients in which the hippocampus is highly sclerotic but also subjects in which the hippocampus appears largely unaffected.[19,20] Both pre-surgery magnetic resonance imaging (MRI) and post-surgery histological analysis show no differences between tissue in these patients and unaffected humans.[19] Such non-sclerotic samples provide a unique opportunity to determine the synaptic basis of memory storage and higher-order computations in the human hippocampus.

RESULTS

Recording from neurons in the human hippocampus

To characterize cells, synapses, and circuits in the human CA3 region, we obtained hippocampal tissue blocks from 17 temporal lobe epilepsy (TLE) patients who underwent unilateral temporal lobe resection surgery[19] (Figure 1). This procedure resulted in the excision of neocortical and hippocampal tissue, which was immediately transferred to the laboratory for acute slice preparation and multicellular patch-clamp-based functional circuit mapping.[14,16,18,21,22] By combining this analysis with post hoc immunohistochemistry, visualization of recorded
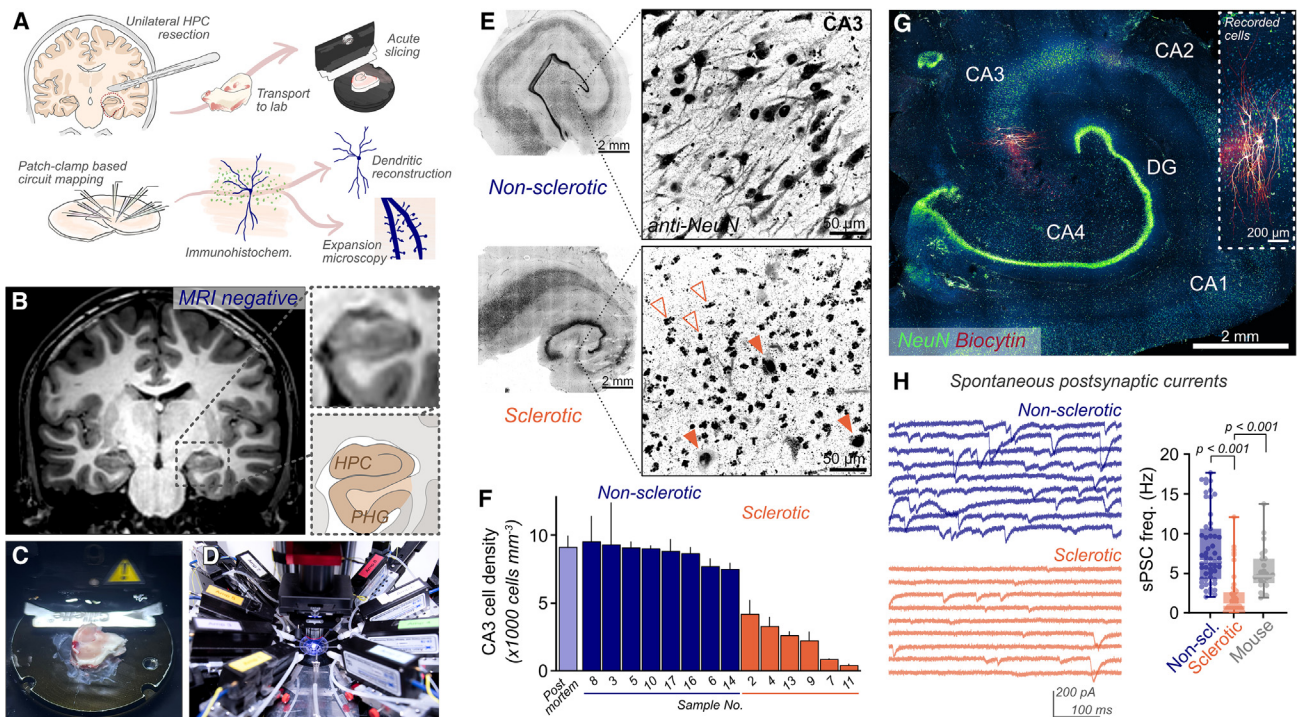
Figure 1. Using human hippocampal tissue from temporal lobe resection

(A) Experimental procedure for analysis of human hippocampal circuits.

(B) Pre-surgery MRI brain image depicting tissue to be excised (schematic colored; HPC, hippocampus, PHG, parahippocampal gyrus).

(C) Hippocampal tissue block during sectioning to acute slices.

(D) Multicellular patch-clamp recording configuration.

(E) Anti-NeuN staining of acute human hippocampal slices. NeuN-positive neuronal remains are observed in sclerotic tissue, showing the extent of disease-induced cell loss. Empty arrowheads denote degenerated neurons, and filled arrowheads indicate putatively healthy neurons.

(F) Substantial and variable reductions in CA3 neuron density were found in sclerotic tissue (orange, a subset of samples presented), while non-sclerotic samples (dark blue) have a stable CA3 cell density (mean ± SEM of 3 slices per sample). Non-sclerotic neuronal densities are comparable to those of non-epileptic postmortem CA3 (light blue, mean ± SEM of 3 donor samples).

(G) Example non-sclerotic recorded slice with anti-NeuN (blue-green LUT) and AF647-conjugated streptavidin to visualize biocytin-filled recorded cells (red; inset, magnified view).

(H) The frequency of sPSCs at CA3 PNs is greatly reduced in sclerotic tissue when compared with non-sclerotic tissue or mouse CA3 PN recordings (left, example voltage-clamp recordings from human CA3 PNs). Line, box, and whiskers depict median, 25th–75th percentiles, and min/max values (mean ± SEM: non-sclerotic human, 8.0 ± 0.6 Hz, n = 55 cells; sclerotic human, 2.2 ± 0.4 Hz, n = 46 cells; mouse, 5.4 ± 0.5 Hz, n = 26 cells; Kruskal-Wallis test, p < 0.0001).

See also Figure S1.

neurons, and expansion-based superresolution microscopy, we performed a detailed structural and functional characterization of the CA3 recurrent network in the human brain (Figures 1A–1D).

Pre-surgery MRI analysis, infrared differential interference contrast (IR-DIC) imaging during slice recording, and post hoc immunohistochemical quantification of neuronal densities demonstrated that the population of patients was highly heterogeneous. 9 of 17 hippocampal tissue samples showed sclerosis, with size reductions visible before surgery ("MRI-positive") and neuronal loss seen in tissue samples across the CA subfields, including CA3 (Figure 1E).[23] By contrast, the remaining samples showed no signs of hippocampal sclerosis ("MRI-negative") (Figures 1B and 1E). Clinical histology analysis classed all these samples as lacking hippocampal sclerosis and reported equivalent hippocampal cell densities and tissue structure to non-epileptic human samples (Table S1). We quantified cell density in CA3 and confirmed a high and stable density level in non-scle-

rotic samples, equivalent to that of non-epileptic postmortem samples (Figures 1F and S1A). Furthermore, the frequency of spontaneous postsynaptic currents (sPSCs) at recorded CA3 pyramidal neurons (PNs) in this "non-sclerotic" tissue was an order of magnitude higher than in sclerotic samples and similar to mouse CA3 PNs, suggesting functionally preserved circuit wiring (Figure 1H). Taken together, these analyses showed no evidence of disease-induced damage to the hippocampal circuitry in non-sclerotic patient tissue, corroborating the suggestion that CA3 is intact. This allowed us to examine the structure and function of human hippocampal microcircuits in the most physiological setting possible.

Sparse synaptic connectivity in human CA3

To probe the functional synaptic connectivity in human CA3, we used multicellular patch-clamp-based circuit mapping. In total, we obtained 56 multicellular recordings from non-sclerotic
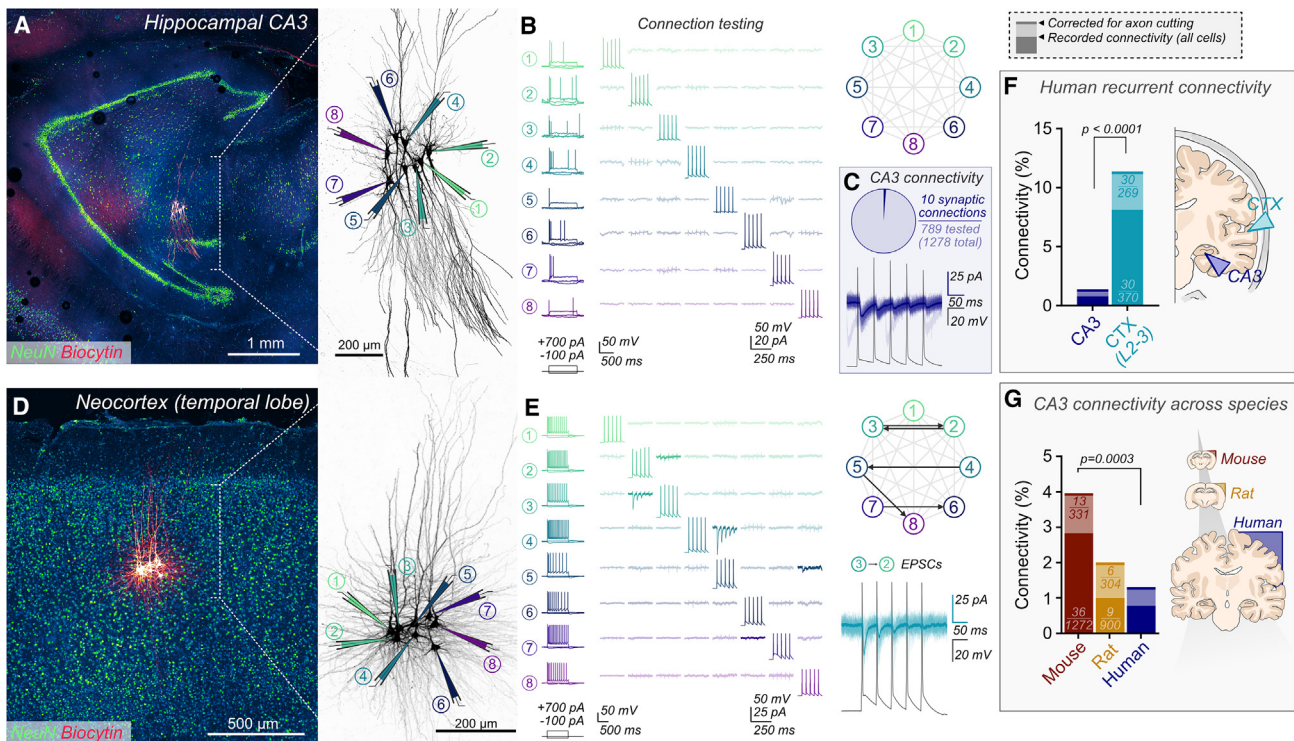
Figure 2. Sparse synaptic connectivity in human CA3

(A) Human acute slice with octuple recording from CA3 (anti-NeuN, blue-green; streptavidin-biocytin staining, red), with magnified view of recorded CA3 PNs (right) and annotated recording pipettes.

(B) Action potential phenotype (left) and connectivity testing (right) for cells recorded in (A). Averaged current traces in response to presynaptic cell spiking (diagonal) are shown.

(C) CA3 PN connectivity is low in human tissue (10/1,278 tested connections, 10/789 connections after axon correction; 0.5 mm visible axon required for inclusion as a presynaptically tested neuron). Example of synaptic connection between human CA3 PNs is depicted. Presynaptic cell spiking (gray) is followed by reliable postsynaptic currents (individual traces overlaid with the average response).

(D) Octuple recorded human neocortical neurons (layer 2–3).

(E) Corresponding firing properties and connection testing. Five synaptic connections are observed (bold traces), with connectivity scheme (upper right) and magnified example synapse (lower right) depicted.

(F) Human neocortical L2-3 PN connectivity is an order of magnitude higher than between CA3 PNs (recorded: 30/370 tested connections, corrected: 30/269). Fisher's exact test, $p < 0.0001$ for both recorded and corrected connectivities.

(G) Sparse connectivity is observed in CA3 of both rodents and humans, with decreasing connectivity correlating with increasing brain size (mouse: 36/1,272 tested connections and 13/331 axon corrected; rat: 9/900 tested connections and 6/304 axon corrected). Fisher's exact test for 3 conditions, $p < 0.0001$; mouse vs. human pairwise comparison with Benjamini-Hochberg correction: $p = 0.0003$, total connectivity; $p = 0.027$, corrected connectivity.

See also Figures S2 and S3.

human hippocampal slices (8 octuples, 9 septuples, 7 sextuples, 8 quintuples, 14 quadruples, 7 triples, and 3 pairs across 8 patients; Figures 2A–2C; Tables S1 and S2). From these recordings, 262 neurons were rigorously identified as CA3 PNs by electrophysiological and morphological criteria (Figure S1B). In total, we found 10 putative monosynaptic connections in 1,278 tested CA3 PN pairs, corresponding to a measured local connection probability of 0.78% (Figure 2C). To account for the effects of tissue slicing and to better approximate CA3 connectivity in the intact circuit, we performed a detailed morphological analysis of all recorded neurons and considered only neurons with extensive axonal staining as possible presynaptic partners (> 0.5 mm reconstructable axon; Figure S2; see also Campagnola et al.[8] and Planert et al.[17]). With this refinement, the corrected connection probability was 1.27% (10 out of 789 tested connections).

Intersomatic distance between synaptically connected neurons varied over a wide range, with no evidence for distance dependence (Figure S3A), in contrast to other brain circuits[17] but consistent with CA3 measurements in rodents.[14] These results demonstrate that the human CA3 is a sparse but broadly connected recurrent network. We observed no evidence of directional connectivity on the deep-superficial axis in this dataset (Figure S3B).

Previous studies observed high connectivity between neocortical layer 2–3 PNs in humans (10%–15%[8,16–18,24,25]). To validate that sparse synaptic connectivity in human CA3 resulted from circuit architecture rather than tissue or recording quality, we performed additional multicellular recordings from human layer 2–3 neocortical neurons under identical experimental conditions, using neocortical temporal lobe tissue resected during

hippocampal surgery (Figures 2D and 2E). We found dense recurrent connectivity in the human neocortex (corrected connectivity 11.2%, 30/269 tested connections, data from 2 patients), confirming previous observations,[8,16,17] but in striking contrast to our findings in the human hippocampal CA3 region ($p < 0.0001$; Figure 2F). Thus, sparse connectivity is a specific property of the human hippocampal CA3 circuit, whereas denser connectivity is characteristic for the human neocortex.

Sparse CA3 synaptic connectivity was previously demonstrated in both rats[14] and guinea pigs.[26] However, surprisingly high CA3 connectivity has recently been reported in mice.[27] To quantitatively analyze synaptic connectivity across species, we compared connection probability among humans, rats, and mice (Figures 2G and S3D–S3F). When measured under identical experimental conditions, connectivity was highest in the mouse (measured: 2.83% and corrected: 3.93%), intermediate in the rat (measured: 1.00% and corrected: 1.97%), and lowest in humans (measured: 0.78% and corrected: 1.27%; Figure 2G). Consistent with these findings, the branching density of CA3 axons was lower in humans than rodents (Figure S2B). Therefore, not only does human CA3 employ much sparser connectivity than neocortical recurrent networks, but circuit architecture appears to sparsify across species with increasing brain size. Neocortical connectivity levels are comparable, if not denser, in humans than mice,[8,18] and the formation of dense interconnectivity has been considered a mechanism for "uniquely human networks."[24] Our results suggest that the CA3 recurrent circuit uses a different mechanism to support human cognition.

Reliable and precise synaptic transmission in human CA3

Next, we examined the functional properties of cells and synapses in the human CA3 (Figures 3 and S4). As our current understanding of hippocampal function is almost entirely based on analysis of rodent tissue, we first characterized the basic features of human CA3 PNs. Passive membrane properties of CA3 PNs showed similarities between humans and rodents. Human CA3 neurons showed greater cell capacitance, lower input resistance, and a higher current threshold of action potential (AP) initiation (Figure S4). However, the membrane time constant was similar, indicating that differences were generated by a larger surface area rather than differences in specific membrane properties. Active membrane properties were more distinct. Human CA3 PNs showed broader single APs, more pronounced adaptation, and narrower interspike interval (ISI) distributions during repetitive firing (Figures S4E and S4F). Thus, spiking of CA3 PNs showed a higher degree of temporal precision in humans than in rodents.

We then characterized the properties of unitary synaptic transmission at hippocampal CA3-CA3 synapses (Figure 3). In comparison to the well-characterized neocortical synapses, excitatory postsynaptic potentials (EPSPs) evoked between recorded human CA3 PNs had notably slower rise and decay time (Figure 3B). CA3 PNs showed a markedly slower apparent membrane time constant than neocortical neurons ($p = 0.0002$; Figure 3C), suggesting differences in postsynaptic membrane properties as a potential mechanism. To further distinguish between effects of synaptic conductance and postsynaptic mem-

brane properties, we measured the kinetics of excitatory postsynaptic currents (EPSCs) and found far less kinetic difference than between EPSPs (EPSC rise and decay kinetics: $p = 0.23$ and 0.19, respectively; Figures 3D and 3E). Finally, human CA3 synapses were less depressing than neocortical synapses during 20-Hz train presynaptic stimulation ($p < 0.0001$ for EPSPs and 0.02 for EPSCs; Figures 3B and 3E). Together, therefore, human CA3 PNs provide a broader window for temporal summation. Both the cellular and synaptic properties of CA3 PNs produce a recurrent circuit with greater integrative power in human hippocampal CA3 than in human neocortical layer 2–3. Average depolarizations from unitary CA3-CA3 connections were less than 2 mV, even during train stimulation, and therefore did not generate postsynaptic APs. Input-output conversion in human CA3 will require use of their broad, integrating synaptic properties.

To identify potentially unique properties of synaptic signaling in humans, we analyzed unitary EPSPs and EPSCs in different species (Figures 3F–3H). Direct comparison of mouse and human CA3 synaptic properties showed similar EPSP and EPSC amplitudes and kinetics across species (Figures 3G and S5). However, there was a major difference in the reliability and amplitude precision of synaptic transmission. Human CA3-CA3 synapses were strikingly reliable, with a success probability of 0.90, while mouse synapses showed a significantly lower success probability (0.62; $p < 0.0001$; Figure 3G). Although the synaptic potency (i.e., the amplitude of successes) was equivalent, the coefficient of variation (CV) of success amplitudes was significantly smaller in humans than in mice (0.36 vs. 0.52; $p = 0.0021$). Both differences were corroborated in voltage-clamp recordings (Figures S5A–S5C). Analysis of reliability and amplitude precision of human neocortical synapses revealed that potency, success probability, and CV of successes were not significantly different to human CA3 (Figure S5F). Taken together, human synapses show much lower synaptic fluctuations than mouse synapses, with both greater reliability and precision. Reliable and precise transmission appears to be a general feature of synaptic signaling in human recurrent networks.[28] Therefore, our recordings identify potentially unique functional properties employed by the human brain.

Scaling of recurrent connectivity from mice to humans

Which factors determine sparse synaptic connectivity in the human CA3? In a broad, random network,[29] connectivity can be estimated anatomically as the number of inputs per cell (N_{inputs}), divided by the total number of cells in the network (N_{cells}). Thus, connectivity would be predicted to be proportional to N_{inputs} but inversely proportional to N_{cells}. We tested these predictions in the CA3 network (Figure 4). Stereology analyses indicated that CA3 contains ~110,000 CA3 PNs per hemisphere in mouse,[30] ~300,000 CA3 PNs per hemisphere in rat,[30,31] and ~1.7 M CA3 PNs per hemisphere in humans[32–36] (see STAR Methods). Therefore, human CA3 has undergone a massive evolutionary expansion in cell number[2] (see also Figure 5A).

We next attempted to directly measure N_{inputs} (Figure 4). The size of the neuronal dendritic arbor is known to expand from rodents to humans,[37,38] but the contribution of scaling to CA3 function is unknown. We analyzed the dendritic arbors of
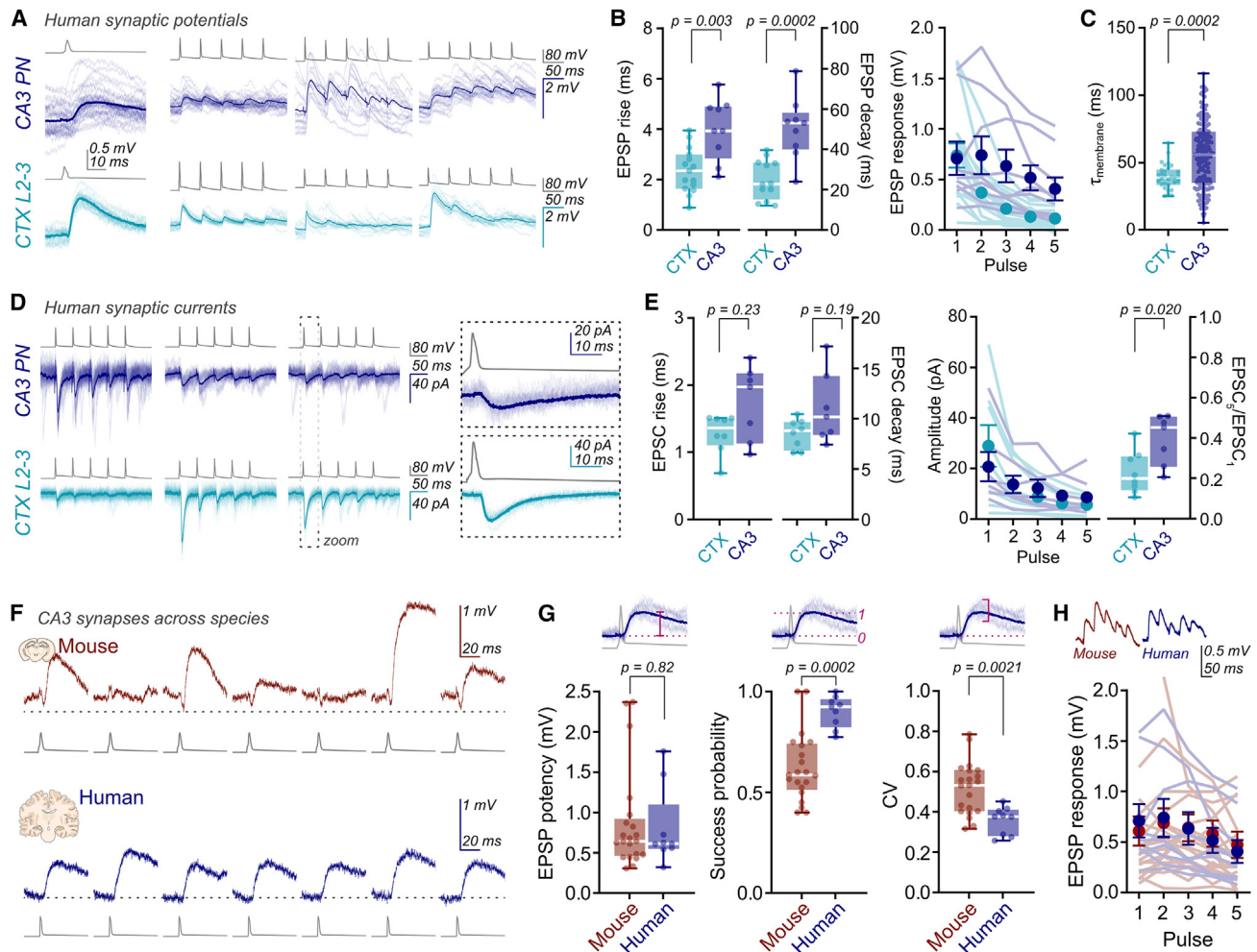
Figure 3. Reliable and precise synaptic transmission in human CA3

(A) Unitary connections between human CA3 or neocortical layer 2–3 neurons (CTX; traces show individual sweeps overlaid with average response).

(B) Synaptic events show a slower time course in human CA3 than in human neocortical layer 2–3 (line, box, and whiskers depict median, 25th–75th percentiles, and min/max values; left, EPSP 20%–80% rise time: CTX, 2.4 ± 0.2 ms, $n = 15$; CA3, 4.0 ± 0.4 ms, $n = 9$; Mann-Whitney test, $p = 0.003$. Right, EPSP decay time constant: CTX, 25.1 ± 2.8 ms, $n = 12$; CA3, 50.6 ± 5.1 ms, $n = 9$; Mann-Whitney test, $p = 0.0002$). The resulting EPSP response to 20-Hz train stimulation is less depressing in CA3 (right, $EPSP_5/EPSP_1$ ratio: CTX, 0.16 ± 0.03, $n = 15$; CA3, 0.58 ± 0.12, $n = 9$; Mann-Whitney test, $p < 0.0001$).

(C) EPSP kinetics reflect the slower membrane time constant of large, integrating CA3 PNs (CTX, 39.7 ± 1.7 ms, $n = 30$ cells; CA3, 55.9 ± 1.8 ms, $n = 185$ cells; Mann-Whitney test, $p = 0.0002$).

(D) Unitary EPSCs from human slices.

(E) EPSC kinetics are comparable between areas (left, EPSC 20%–80% rise time: CTX, 1.3 ± 0.1 ms, $n = 8$; CA3, 1.7 ± 0.2 ms, $n = 7$; Mann-Whitney test, $p = 0.23$; EPSC decay time constant: CTX, 8.5 ± 0.5 ms, $n = 8$; CA3, 11.0 ± 1.3 ms, $n = 7$; Mann-Whitney test, $p = 0.19$), while CA3 synapses are less depressing than neocortical synapses (right, $EPSC_5/EPSC_1$ amplitude ratio: CTX, 0.23 ± 0.04, $n = 8$; CA3, 0.39 ± 0.05, $n = 7$; Mann-Whitney test, $p = 0.020$).

(F) Example sweeps from a CA3 synapse of mouse (upper, red) and human (lower, blue).

(G) Similar potency was found in both species (mouse, 0.87 ± 0.14 mV, $n = 21$; human, 0.80 ± 0.16 mV, $n = 9$; Mann-Whitney test, $p = 0.82$), yet human synapses are substantially more reliable, with minimal synaptic failures (probability of success: mouse, 0.62 ± 0.04, $n = 21$; human, 0.90 ± 0.03, $n = 9$; Mann-Whitney test, $p = 0.0002$), and less variation in the amplitude of successes (coefficient of variation, CV: mouse, 0.52 ± 0.03, $n = 21$; human, 0.36 ± 0.02, $n = 9$; Mann-Whitney test, $p = 0.0021$).

(H) Average responses to 20-Hz trains are similar between species.

See also Figures S4 and S5.

human CA3 neurons by confocal microscopy and reconstruction (Figures 4A–4D). Human neurons were highly heterogeneous, having either one or two apical dendrites, and some neurons displayed extreme basal dendrite extension or apparently "inverted" topology (Figure 4B). To determine the cable length

contributing to the CA3 recurrent system, we considered dendrites covered by simple spines in *stratum oriens* and *stratum radiatum*, while excluding proximal dendrites decorated by thorny excrescences (mossy fiber input) and distal dendrites entering *stratum lacunosum-moleculare* (perforant path input). In a subset
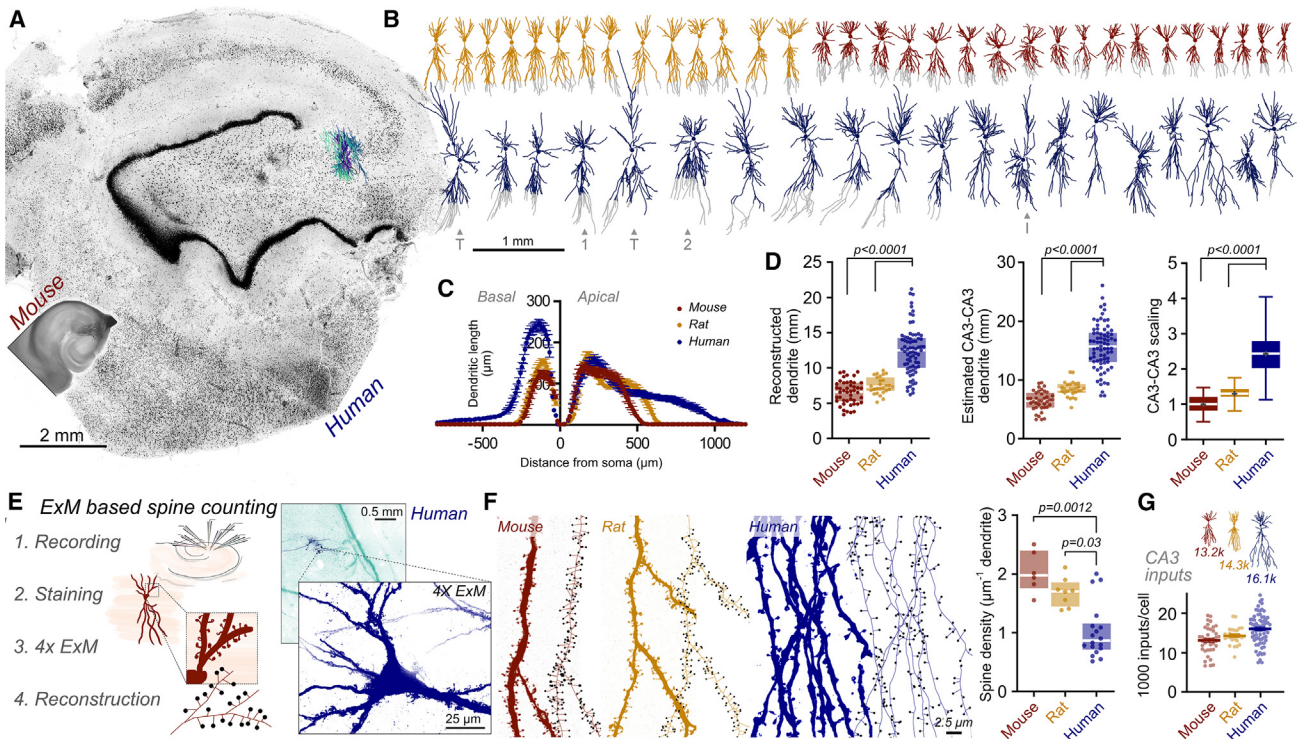
Figure 4. Human CA3 PNs have longer dendrites but lower spine density

(A) Human and mouse slice images demonstrate the expansion in hippocampal size in humans. NeuN-stained human tissue (confocal) is depicted to scale with a DAB-stained mouse slice. Reconstructed human neurons are depicted (colored).

(B) Array of reconstructed mouse (red), rat (yellow), and human (blue) CA3 PN skeletons, demonstrating cell size expansion across species. Somata are depicted as circles, while dendrites not likely to be contributing to the CA3 recurrent circuit are colored gray. Neurons with one ("1") or two ("2") apical dendrites, putative inverted topology (i.e., reversed direction of basal and apical dendrites, "I"), or with an elongated "taproot" basal dendrite ("T") are indicated.

(C) Quantified dendritic length with respect to the soma (zero) for reconstructed rodent and human neurons shows an increase in the length and abundance of basal dendrites in human CA3 PNs but predominantly an extension in length of human apical dendrites (mouse, $n = 33$; rat, $n = 27$; human, $n = 57$ cells).

(D) The total dendritic length of reconstructed human CA3 PNs is greater than that of rodent PNs (line, box, and whiskers depict median, 25th–75th percentiles, and min/max values; left, mean ± SEM: mouse, 6.5 ± 0.2 mm, $n = 46$ cells; rat, 7.5 ± 0.2 mm, $n = 27$ cells; human, 12.5 ± 0.4 mm, $n = 73$ cells; Kruskal-Wallis test, $p < 0.0001$), with a corresponding extension of dendritic length predicted to form the CA3 recurrent circuit (center: mouse, 6.5 ± 0.3 mm, $n = 39$ cells; rat, 8.5 ± 0.2 mm, $n = 27$ cells; human, 15.7 ± 0.5 mm, $n = 73$ cells; Kruskal-Wallis test, $p < 0.0001$). Species-scaled dendritic length (normalized to mouse) shows an approximately 2.5-fold increase in dendrite for the CA3 recurrent system of human PNs over mouse neurons (right, mean marked as +; mean ± SEM: mouse, 1.00 ± 0.04, $n = 39$ cells; rat, 1.31 ± 0.04, $n = 27$ cells; human, 2.42 ± 0.07, $n = 73$ cells; Kruskal-Wallis test, $p < 0.0001$).

(E) 4× expansion microscopy (ExM) approach for analysis of spine density (left) and recorded human slice (right: anti-NeuN, green; biocytin-filled cells, blue) with ExM image of human CA3 PN showing detailed morphology of dendritic spines and thorny excrescences. Scale bar indicates pre-expansion size.

(F) Imaged and reconstructed dendrites and spines (circles) from CA3 PN dendrites. Scale bar indicates pre-expansion specimen size. The density of dendritic spines on human CA3 dendrites is lower than mouse dendrites (mean ± SEM: mouse, 2.04 ± 0.14 spines μm^{-1}, $n = 6$ cells; rat, 1.69 ± 0.09 spines μm^{-1}, $n = 8$ cells; human, 1.03 ± 0.11 spines μm^{-1}, $n = 18$ cells (6 patients); Kruskal-Wallis test, $p = 0.0005$).

(G) The estimated CA3 recurrent inputs per neuron (estimated CA3 dendrite length × mean spine density) increase only minimally from mice to humans (mouse: 13,200; rat: 14,300; human: 16,100 inputs per cell).

See also Figures S6 and S7.

of CA3 PNs, we observed that dendrites crossed the granule cell (GC) layer (Figure S1C), which we also presumed to receive perforant path input. We corrected for dendritic cutting by calculating the expected length of all dendrites terminating at the slice surface. Total dendritic length receiving CA3 input increased from 6.5 mm per PN in mice up to 15.7 mm in humans (Figure 4D); therefore, cell size expansion resulted in a 2.42 ± 0.07-fold extension of CA3 recurrent dendritic length per cell from mice to humans.

We then counted dendritic spines on the relevant dendritic branches (Figures 4E–4G). Individual spines are difficult to un-

equivocally determine with diffraction-limited light microscopy. Therefore, we optimized a 4× expansion microscopy (ExM) protocol (4× ProExM[39]) that enabled superresolution analysis of dendritic architecture from recorded neurons (Figure 4E). Using this protocol, biocytin-streptavidin-labeled neurons in previously fixed and cleared human tissue could be expanded and imaged at 4× increased resolution even 1 year after initial sample mounting. We could visualize both thorny excrescences and simple spines on primary dendrites of human CA3 neurons (Figures 4E and 4F). Simple spines (recurrent collateral input) occurred at similar densities on both basal and apical dendrites
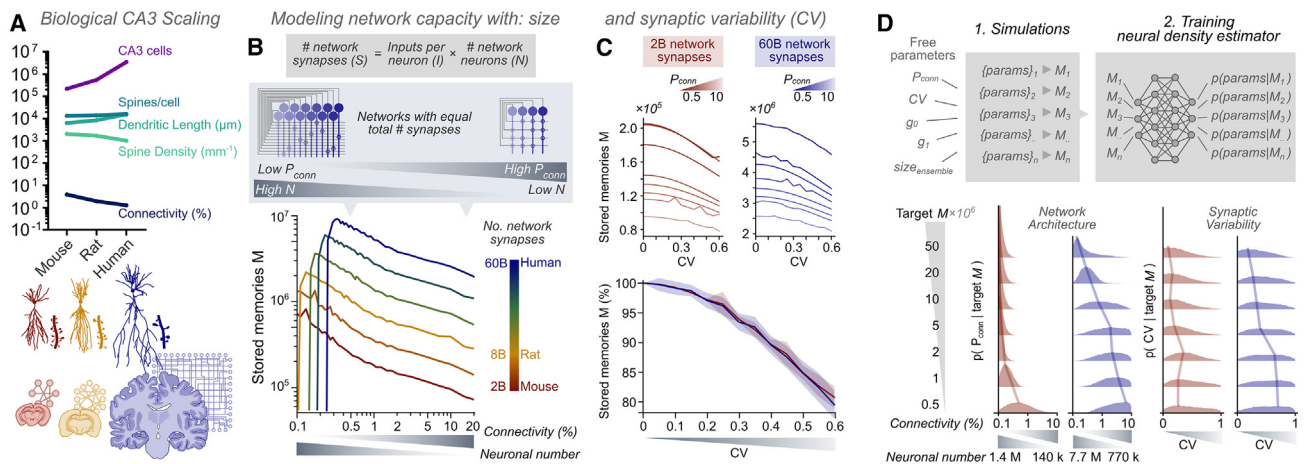
Figure 5. Sparse connectivity and reliable synaptic signaling increase memory storage capacity of a CA3 network model

(A) Measured scaling of CA3 network parameters across species.

(B) Theoretical CA3 network models with fixed numbers of total synapses in the network (variable number of nodes and inputs per node) show maximal pattern storage and retrieval with lower connectivity (high N) than with higher connectivity (low N). This applies to networks of all sizes, equivalent to biological CA3 networks across species (colored).

(C) Adding variability to synaptic transmission (increasing CV) reduces the memory storage capacity of networks of all sizes (upper). Networks (from B) with varying connectivities (shades) show equivalent effects. This reduction occurs by an equivalent proportion, as evident from normalized data (lower). Lines and shading represent mean and SD of normalized capacity for networks with different structures of equivalent size (colored).

(D) Simulation-based inference (SBI) optimization of CA3 network properties to achieve maximal memory capacities shows peak shifts of optimal parameter distributions to lower connectivity (high N, low P_{conn}) and low CV with increasing memory capacity requirements. Lines follow maxima of distributions. Networks with 2 billion (red) and 60 billion (blue) synapses were tested.

(Figure S6A), but unexpectedly, spine density on human PNs was reduced to just 50% of that on mouse CA3 PNs (Figure 4F). This decreased spine density in human tissue parallels electron microscopy (EM) observations from neocortical PNs,[40] and we could confirm this observation in non-epileptic postmortem CA3 tissue (Figure S6B). Therefore, lower excitatory input density appears to be a conserved feature of excitatory neurons across the human brain.

Based on these results, we estimated the average number of recurrent collateral spines per complete CA3 PN across species, calculating 13,200 spines per CA3 PN in mice, 14,300 in rats, and 16,100 in humans (Figure 4G). Thus, evolutionary expansion of the hippocampus is accompanied by a massive increase in cell number, a substantial increase in dendritic length, and a decrease in spine density, overall leading to a moderate increase in the number of synaptic inputs. Taken together, these results indicate that connectivity in the CA3 circuit is not governed by a simple scaling rule but rather by multiple scaling rules with different slopes and directions (Figure 5A).

Using these numbers, we can predict synaptic connectivity for a theoretical CA3 network (Figure S7A). Assuming that the number of spines equates the number of inputs and that ipsilateral and contralateral inputs contribute equally to synaptic connectivity,[41,42] we predict an average connection probability of 5.99% for mouse, 2.65% for rat, and 0.47% for human (Figure S7A; see STAR Methods for caveats and limitations). These values approximate experimental measurements surprisingly well, in line with the view of CA3 as a broadly connected network and supported by axon arborization patterns across species.[43–46] Interestingly, connectivity levels akin to the

neocortex would only be possible with much more focal connectivity. As a human CA3 PN has only 16.1k inputs, 15% local connectivity would imply that one neuron receives all its input from within 3% of the total human CA3 (~110k neurons; Figure S7B), while 1.3% local connectivity (as measured) broadens this influence to 36% of the network. Therefore, the sparse connectivity we identify in human hippocampal CA3 reflects the mutually exclusive circuit architectures between CA3 and neocortex: sparse and broad connectivity in CA3 vs. dense and "columnar" connectivity in the neocortex.[8,17,18,22,47–49] Such a network arrangement likely maximizes the associative power of the hippocampus, facilitating association between parallel, spatially separated information streams.

Theoretical determinants of maximal network capacity

Our results reveal key characteristics of human CA3 circuits: sparse connectivity and reliable synaptic signaling. We sought to understand the influence of these properties on memory storage capacity, using an established theoretical model of CA3 memory function[14,50,51] (Figure 5). In this Hopfield-type network, patterns were stored by Hebbian synaptic plasticity and retrieved from incomplete or degraded versions by pattern completion. Evolutionary expansion of CA3 could have adopted alternative routes: increasing connectivity and consequently input number per neuron, or preferring sparser connectivity (P_{conn}) between greater neuronal numbers (N). To test the efficiency of these options for memory storage, we analyzed networks with a constant total number of synapses, changing connectivity and cell number reciprocally (Figure 5B). Thus, we tested the theoretical pattern storage capacity of small, densely connected networks (high

P_{conn}, low N) up to large, sparsely connected networks (low P_{conn}, high N) (Figure 5B). This approach allows more appropriate comparison of different network structures, surpassing comparisons between networks with equivalent N but differing P_{conn}, which will have vastly different synapse numbers. Capacity of the network was measured as the maximal number of random patterns that could be stored without interfering with reliable recall of previous patterns.

Recurrent networks of all sizes, from 2 billion total synapses (approximating mouse CA3) to 60 billion total synapses (approximating human CA3), consistently showed greater storage capacity for lower connectivity combined with higher cell number than for higher connectivity combined with lower cell number, except at unrealistically low connectivity values, in which networks were silent due to insufficient recurrent activity (Figure 5B). Therefore, for a theoretical CA3 network, an evolutionary drive for improved memory capacity would prioritize expansion of neuronal number over an increase in network interconnectivity. We extended this analysis to examine the effect of synaptic reliability on pattern storage. Increasing synaptic variability (CV) reduced the memory storage capacity for networks of all sizes in a proportional manner (Figure 5C). Together, our results suggest that maximal storage capacity in a theoretical recurrent network is achieved by sparse connectivity, increasing neuronal number rather than each neuron's input number, and enhancing synaptic reliability. These properties match those we experimentally recorded in human CA3.

To test whether our conclusions hold more generally, we performed a further analysis avoiding any need to constrain model parameters (P_{conn}, CV, ensemble size, threshold [g_0], and inhibition [g_1]; Figure 5D). This "simulation-based inference" approach (SBI[52,53]) is based on Bayesian inference and uses model simulations with arbitrary parameter values to train a neural density estimator, which can subsequently compute the distribution of parameters most likely to reach a given memory capacity value M. Using this unbiased approach, when increasing the target value of M, we observed consistent shifts in the peak of distributions to smaller values of both connectivity and CV in both small and large networks (Figure 5D). Therefore, achieving maximal network capacity is most likely with high neuronal numbers, sparse connectivity, and reliable synaptic transmission. These results corroborate the idea that the human CA3 follows an efficient coding design, maximizing associational power and memory storage capacity.

Pathway-specific expansion of CA3 synaptic inputs

Our results suggest that CA3 recurrent connectivity shows sparsification from mice to humans. To test whether evolutionary sparsification is synapse-specific, we examined connectivity in the mossy fiber pathway, which relays input from dentate gyrus GCs (Figure 6). While the basic signaling properties of human mossy fiber synapses have been determined,[54] the rules of their connectivity in humans remain unknown. As with CA3 PNs, GC numbers show substantial evolutionary expansion, from ~460,000 GCs per hemisphere in mice[55,56] to ~15 M per hemisphere in humans.[33–35] Compared with the well-known rodent hippocampal architecture, the human GC layer has greatly extended in length, maintaining a thin layer with a high GC den-

sity. By contrast, the CA3 layer has fanned out along the deep-superficial axis (Figures 1G, 6A, and 6B). The clear separation between mossy fiber tract (*stratum lucidum*) and cell body layer (*stratum pyramidale*) observed in mice has been lost in human CA3, with PN somata and mossy fibers intermingled[32,57] (Figure 6B). As a result, we observed thorny excrescences on both apical and basal dendrites of human CA3 PNs, implying that mossy fiber input occurs on a wider range of subcellular domains of postsynaptic target cells (Figures 6A and 6B; see also Lauer and Senitz[58] and Lu et al.[59]).

The length of thorny dendrite on reconstructed PNs increased 8.2 ± 0.5-fold from mice to humans, supra-proportional to both total dendritic length and dendritic length of the CA3 recurrent collateral system (2.4 ± 0.1-fold increase; Figure 6C). To confirm that thorny dendrites were indeed the target of mossy inputs in human tissue, we applied LICONN (light-microscopy-based connectomics),[60] an iterative hydrogel-expansion technology, enabling synapse-level tissue reconstruction. An effective spatial resolution of <20 nm laterally (~16-fold increased over confocal imaging) with high-fidelity tissue preservation and comprehensive structural labeling (pan-protein) allowed us to reconstruct the mossy fiber connectome of PN dendrites, which displayed abundant large boutons contacting thorny excrescences in both mouse and human (Figure 6D). We observed multi-bouton contacts at this synapse in human tissue, which were not seen in other species (Figure S8). Bouton density was reduced by 30% on human PNs compared with mice (0.53 vs. 0.75 boutons per μm dendritic length in humans vs. mice; $p = 0.023$; Figure 6E). While this is a further example of lower excitatory input density in human tissue, this effect is eclipsed by the massive expansion in thorny dendritic length. We estimated that a human CA3 PN receives on average ~280 GC mossy fiber inputs, in comparison with ~50 for a mouse CA3 PN (see also Amaral et al.[61]; Figure 6E). At the level of GC-CA3 connectivity, these values correspond to 0.011% and 0.002% of GCs connecting to each CA3 PN in mice and humans, respectively, suggesting that network connectivity is sparser at both GC and CA3 recurrent inputs to the human CA3 area. At the single-cell level, however, human CA3 PNs experience a much greater level of GC innervation to those of the mouse brain. As a proposed key function of CA3 is association of incoming dentate gyrus input streams,[62] this striking expansion of human mossy fiber convergence has the potential to substantially increase the associational power of human CA3.

DISCUSSION

Until now, only limited characterization of the functional properties of cells, synapses, and circuits in the human hippocampus has been performed.[7,54,63–66] It is often assumed that the mechanisms of synaptic signaling and information processing are conserved across species and that investigating basic mechanisms in model organisms will provide insights into higher cognitive functions in humans. However, a proof for this assumption is lacking. Here, we have tackled this question and present functional microcircuit properties of the human hippocampal CA3 region, the largest autoassociative network in the brain, which plays a key role in learning, memory, and higher-order
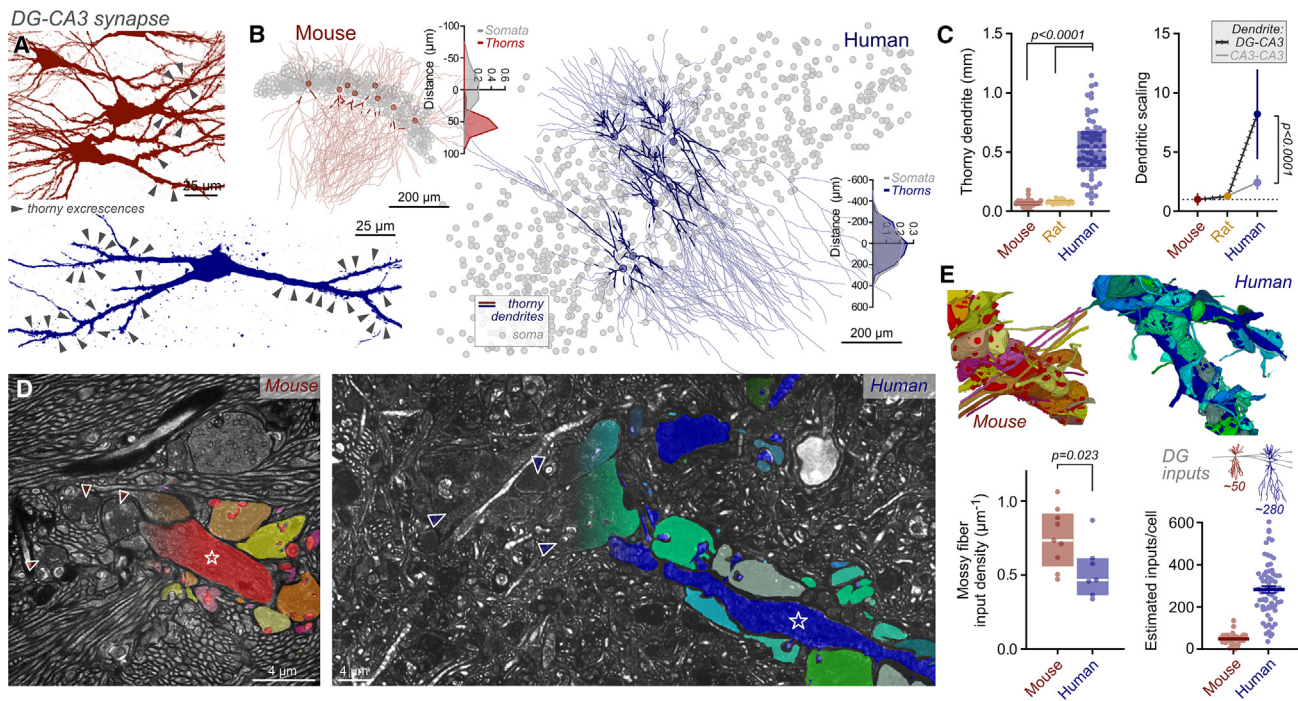
Figure 6. Expanded mossy-fiber-CA3 input in the human brain

(A) Both mouse (upper) and human (lower) CA3 PNs display complex spines on primary apical dendrites of biocytin-labeled cells ("thorny excrescences," arrowheads).

(B) Left, thorny dendrites of mouse neurons (bold lines on cell reconstructions) segregate from the pyramidal cell layer (somata, gray circles). Right, human thorny dendrites overlap with the expanded *stratum pyramidale* and extend throughout the somatic layer. Relative frequency histograms depict distributions of somata (gray) and thorny dendrites (colored).

(C) Length of reconstructed thorn-covered dendrite is expanded in humans compared with mouse CA3 PNs (line, box, and whiskers depict median, 25th–75th percentiles, and min/max values; mouse, 0.065 ± 0.005 mm, $n = 39$; rat, 0.082 ± 0.003 mm, $n = 27$; human, 0.54 ± 0.03 mm, $n = 67$; Kruskal-Wallis test, $p < 0.0001$), equating to a 8-fold increase in dendritic coding space (left, absolute values; right, normalized to mouse mean length, mean $\pm$ SD presented; human dendritic scaling: thorny dendrite, 8.2 ± 3.8; CA3 dendrite, 2.4 ± 0.6; Mann-Whitney test, $p < 0.0001$).

(D) LICONN-based tissue imaging allows reconstruction of thorny dendrite (starred) and contacting mossy fiber boutons (indicated with triangles or colored segmentation; scale bar reflects pre-expansion length). Segmentation is included on half of images for presentation of raw data.

(E) Examples of 3D reconstructed dendrites with mossy fiber boutons. While bouton density appears lower in human tissue (boutons per unit length of thorny dendrite: mouse, 0.75 ± 0.07 μm^{-1}, $n = 9$ cells; human, 0.53 ± 0.07 μm^{-1}, $n = 7$ cells from 2 patients; Mann-Whitney test, $p = 0.023$), estimated number of GC inputs per CA3 PN (recorded thorny dendrite length × mean input density) substantially increases in the human brain (error bars depict SEM; mouse, 49 ± 4; human, 282 ± 16).

See also Figure S8.

computations. This study reports the properties of synaptically connected pairs of neurons in the human hippocampus, revealing specific features of these connections that could only be observed through direct analysis of human brain tissue.

We demonstrate that connectivity of human CA3 cannot be predicted from the rodent brain by a simple scaling rule. First, connectivity differentially scales across circuits. In the neocortex, connectivity increases from mice to humans,[8,17,18] whereas in hippocampal CA3 we observed a decrease. Second, discrete CA3 microcircuit properties change following diverse scaling relations, with different dependencies for neuron numbers (increase from mouse to human), dendritic length (increase), and input density (decrease). Finally, we found that the different hippocampal inputs to CA3 PNs do not expand uniformly, exhibiting distinct changes in recurrent collaterals and mossy fiber inputs. We observe a decrease in excitatory input density between mice and humans at two hippocampal synapses. This parallels a similar observation in the neocortex[40] (Figures 4F and 6E), suggesting it may be a wider principle of human PN architecture.

Our results reveal that the functional properties of unitary synaptic transmission in humans are distinct from those in rodents. Human CA3-CA3 recurrent synapses show reliable transmission, with a high proportion of successes and a small CV of success amplitude. This is different from rodents, where transmission at these synapses is unreliable.[67] Higher synaptic reliability has also been suggested in human neocortical layer 2–3 synapses,[28] and therefore may also be a wider principle of human synaptic transmission. Whether this reliability is related to broader APs (Figure S4) or lower spine density in human circuits (Figure 4F), implying a larger distance between adjacent synapses, remains to be addressed.

Our results provide evidence that the specific properties of human CA3 have major advantages, increasing the computational

power of the network. Classical models of the hippocampal CA3 region suggest that incoming information is transferred by hippocampal mossy fiber synapses, which induce association and storage of information in CA3-CA3 synapses by Hebbian synaptic plasticity.[62,68] Our results indicate that specialization of both synapses in the human brain may be critical for network performance. The extension of the mossy fiber termination zone may allow single cells to respond to a much larger number of synaptic input combinations, increasing the power of single-neuron computations. This could substantially enhance the ability of the network to perform pattern separation computations and to participate in combinatorial encoding.

The parallels between anatomy-based theoretical connectivity and measured connectivity support the view of CA3 as a sparse and broadly connected recurrent network. Although the agreement between predicted and measured connectivity is remarkable (Figure S7A), it is important to note caveats in this comparison. First, anatomical connectivity based on spine counting can only be a proxy for true functional connectivity. If increased excitatory input onto PN dendritic shafts occurs in human hippocampus as it does in the neocortex,[40] this would cause underestimation of input levels, while synapses involving multiple spines would cause overestimation. Neocortical neurons have a mean of 1.6 synaptic contacts per connection.[69] Multi-contact synapses have been suggested to occur in CA3,[14] but connectomic analysis of CA3 axons in CA1 shows almost exclusively a single input per spine.[70–72] Finally, a proportion of synapses in the brain may be functionally silent,[73,74] again causing overestimations of functional connectivity from structural data. Together, spine density is likely to be a good approximation of the number of CA3 presynaptic neurons in the recurrent circuit but is not a definitive measure. In addition, potential cell-specific wiring[45,75] within the CA3 PN network and incomplete coverage of the entire hippocampus by individual CA3 PN axons will differentiate biological CA3 from a random network.

Although hippocampal PN populations were historically assumed to be uniform, evidence for genetic, morphological, and functional heterogeneity has accumulated.[76,77] In rodent CA3, PN subclasses segregate along the deep-superficial axis, with distinct burst-firing properties and extent of dentate gyrus innervation.[75,78,79] Our data show substantial heterogeneity in morphology, active properties, and thorny dendrite length among human CA3 PNs. We did not observe clearly segregated subclasses or any evidence of completely thorn-lacking cells.[78] Thus, the correspondence between human and rodent PN subclasses requires further investigation. However, we did observe indications of possible human-specific CA3 PN subtypes. PNs with an "inverted" morphology with respect to *stratum pyramidale* may reflect the more disorganized "corticalization" of the human hippocampus,[37] while PNs with highly elongated "taproot" basal dendrites (Figure 4B) are reminiscent of human cortical "Betz cells."[80] How these cells and their properties relate to human hippocampal function remains to be studied.

Together, our data suggest that the human hippocampus has followed an efficient coding route of expanding neuronal number. Employing sparse but broad CA3-CA3 connectivity will improve pattern completion and allow the system to associate engrams in a distributed, hippocampus-wide manner. This is fundamentally different from the neocortex, in which dense connectivity within cortical modules or columns may enable fast and efficient local computations.[24] Our results reveal distinct features of microcircuit function of the human hippocampus. While model organism research provides the backbone to understand our brain's function, direct measurements from human brain tissue are essential to reveal the full picture.

Limitations of the study

Our results were obtained from structurally unaffected human tissue, providing the closest possible approximation of the physiological human brain. However, the tissue inevitably comes from patients with TLE, which must be taken into account. Although our results were consistent across patients with different disease background, including a patient with a cavernoma in which the hippocampal structure appeared completely normal (Table S1), and were supported by analysis of postmortem tissue, more work on completely unaffected human samples will be required in the future. Another limitation of human tissue study is the low availability of specimens, resulting in lower sampling and greater variability of estimates than can be achieved using classical model organisms. We have sampled both electrophysiological and morphological properties from a broad population of patients (Table S2), but because of low tissue availability and sparse connectivity, measurements of synaptic properties were unavoidably derived from a small number of patients. It is also important to note that morphological and functional measurements presented here only capture "local" connectivity. The full connectivity across the entire human hippocampus, including long-range and contralateral projections, must be revealed using future technologies. Finally, our study explores the differences between rodent and human hippocampal circuits. Whether the properties and differences we observe are specific to human tissue or are evolutionarily conserved among other closely related species remains unknown without broader sampling of species.

AUTHOR CONTRIBUTIONS

J.F.W. and P.J. conceived the project. J.F.W., V.V.-B., R.J.M.-M., and M.R.T. performed experiments and analyzed data. K.R. performed epilepsy surgery. A.N.-O. performed modeling. J.G.D. contributed to expansion microscopy analysis. M.T. provided clinical support. J.F.W. and P.J. wrote the paper and acquired funding for the project. All authors jointly revised the paper.

DECLARATION OF INTERESTS

M.R.T. and J.G.D. are inventors on a patent application covering expansion microscopy technology.

STAR★METHODS

Detailed methods are provided in the online version of this paper and include the following:

- KEY RESOURCES TABLE
- EXPERIMENTAL MODEL AND STUDY PARTICIPANT DETAILS
  - Human patient tissue samples
  - Human postmortem tissue samples
  - Animals
- METHOD DETAILS
  - Human patient sample acquisition
  - Preparation of human tissue slices
  - Rodent acute slice preparation
  - Postmortem tissue handling
  - Electrophysiology
  - Immunohistochemistry
  - Morphological analysis
  - Expansion microscopy for spine density measurement
  - Caveats of anatomical connectivity predictions
  - Expansion microscopy for synapse reconstruction (LICONN)
  - Estimates of neuronal numbers
  - Mathematical modeling of CA3 function
- QUANTIFICATION AND STATISTICAL ANALYSIS

SUPPLEMENTAL INFORMATION

Supplemental information can be found online at https://doi.org/10.1016/j.cell.2024.11.022.

REFERENCES

1. DeFelipe, J. (2011). The evolution of the brain, the human nature of cortical circuits, and intellectual creativity. Front. Neuroanat. 5, 29. https://doi.org/10.3389/fnana.2011.00029.

2. Herculano-Houzel, S., Catania, K., Manger, P.R., and Kaas, J.H. (2015). Mammalian brains are made of these: A dataset of the numbers and densities of neuronal and nonneuronal cells in the brain of glires, primates, scandentia, eulipotyphlans, afrotherians and artiodactyls, and their relationship with body mass. Brain Behav. Evol. 86, 145–163. https://doi.org/10.1159/000437413.

3. Eyal, G., Verhoog, M.B., Testa-Silva, G., Deitcher, Y., Lodder, J.C., Benavides-Piccione, R., Morales, J., DeFelipe, J., de Kock, C.P., Mansvelder, H.D., et al. (2016). Unique membrane properties and enhanced signal processing in human neocortical neurons. eLife 5, e16553. https://doi.org/10.7554/eLife.16553.

4. Beaulieu-Laroche, L., Brown, N.J., Hansen, M., Toloza, E.H.S., Sharma, J., Williams, Z.M., Frosch, M.P., Cosgrove, G.R., Cash, S.S., and Harnett, M.T. (2021). Allometric rules for mammalian cortical layer 5 neuron biophysics. Nature 600, 274–278. https://doi.org/10.1038/s41586-021-04072-3.

5. Beaulieu-Laroche, L., Toloza, E.H.S., van der Goes, M.-S, Lafourcade, M., Barnagian, D., Williams, Z.M., Eskandar, E.N., Frosch, M.P., Cash, S.S., and Harnett, M.T. (2018). Enhanced dendritic compartmentalization in human cortical neurons. Cell 175, 643–651.e14. https://doi.org/10.1016/j.cell.2018.08.045.

6. Gidon, A., Zolnik, T.A., Fidzinski, P., Bolduan, F., Papoutsi, A., Poirazi, P., Holtkamp, M., Vida, I., and Larkum, M.E. (2020). Dendritic action potentials and computation in human layer 2/3 cortical neurons. Science 367, 83–87. https://doi.org/10.1126/science.aax6239.

7. Mertens, E.J., Leibner, Y., Pie, J., Galakhova, A.A., Waleboer, F., Meijer, J., Heistek, T.S., Wilbers, R., Heyer, D., Goriounova, N.A., et al. (2024). Morpho-electric diversity of human hippocampal CA1 pyramidal neurons. Cell Rep. 43, 114100. https://doi.org/10.1016/j.celrep.2024.114100.

8. Campagnola, L., Seeman, S.C., Chartrand, T., Kim, L., Hoggarth, A., Gamlin, C., Ito, S., Trinh, J., Davoudian, P., Radaelli, C., et al. (2022). Local connectivity and synaptic dynamics in mouse and human neocortex. Science 375, eabj5861. https://doi.org/10.1126/science.abj5861.

9. Molnár, G., Rózsa, M., Baka, J., Holderith, N., Barzó, P., Nusser, Z., and Tamás, G. (2016). Human pyramidal to interneuron synapses are mediated by multi-vesicular release and multiple docked vesicles. eLife 5, e18167. https://doi.org/10.7554/eLife.18167.

10. Molnár, G., Oláh, S., Komlósi, G., Füle, M., Szabadics, J., Varga, C., Barzó, P., and Tamás, G. (2008). Complex events initiated by individual spikes in the human cerebral cortex. PLOS Biol. 6, e222. https://doi.org/10.1371/journal.pbio.0060222.

11. Testa-Silva, G., Verhoog, M.B., Linaro, D., de Kock, C.P.J., Baayen, J.C., Meredith, R.M., De Zeeuw, C.I., Giugliano, M., and Mansvelder, H.D. (2014). High bandwidth synaptic communication and frequency tracking in human neocortex. PLOS Biol. 12, e1002007. https://doi.org/10.1371/journal.pbio.1002007.

12. Lisman, J.E. (1999). Relating hippocampal circuitry to function: recall of memory sequences by reciprocal dentate-CA3 interactions. Neuron 22, 233–242. https://doi.org/10.1016/s0896-6273(00)81085-5.

13. Treves, A., and Rolls, E.T. (1994). Computational analysis of the role of the hippocampus in memory. Hippocampus 4, 374–391. https://doi.org/10.1002/hipo.450040319.

14. Guzman, S.J., Schlögl, A., Frotscher, M., and Jonas, P. (2016). Synaptic mechanisms of pattern completion in the hippocampal CA3 network. Science *353*, 1117–1123. https://doi.org/10.1126/science.aaf1836.

15. Nakashiba, T., Young, J.Z., McHugh, T.J., Buhl, D.L., and Tonegawa, S. (2008). Transgenic inhibition of synaptic transmission reveals role of CA3 output in hippocampal learning. Science *319*, 1260–1264. https://doi.org/10.1126/science.1151120.

16. Peng, Y., Mittermaier, F.X., Planert, H., Schneider, U.C., Alle, H., and Geiger, J.R.P. (2019). High-throughput microcircuit analysis of individual human brains through next-generation multineuron patch-clamp. eLife *8*, e48178. https://doi.org/10.7554/eLife.48178.

17. Planert, H., Mittermaier, F.X., Grosser, S., Fidzinski, P., Schneider, U.C., Radbruch, H., Onken, J., Holtkamp, M., Schmitz, D., Alle, H., et al. (2023). Cellular and synaptic diversity of layer 2–3 pyramidal neurons in human individuals. Preprint at bioRxiv. https://doi.org/10.1101/2021.11.08.467668.

18. Seeman, S.C., Campagnola, L., Davoudian, P.A., Hoggarth, A., Hage, T.A., Bosma-Moody, A., Baker, C.A., Lee, J.H., Mihalas, S., Teeter, C., et al. (2018). Sparse recurrent excitatory connectivity in the microcircuit of the adult mouse and human cortex. eLife *7*, e37349. https://doi.org/10.7554/eLife.37349.

19. Roessler, K., Hofmann, A., Sommer, B., Grummich, P., Coras, R., Kasper, B.S., Hamer, H.M., Blumcke, I., Stefan, H., Nimsky, C., et al. (2016). Resective surgery for medically refractory epilepsy using intraoperative MRI and functional neuronavigation: the Erlangen experience of 415 patients. Neurosurg. Focus *40*, E15. https://doi.org/10.3171/2015.12.FOCUS15554.

20. Lamberink, H.J., Otte, W.M., Blümcke, I., and Braun, K.P.J.; European Epilepsy Brain Bank writing group; study group; European Reference Network EpiCARE (2020). Seizure outcome and use of antiepileptic drugs after epilepsy surgery according to histopathological diagnosis: a retrospective multicentre cohort study. Lancet Neurol. *19*, 748–757. https://doi.org/10.1016/S1474-4422(20)30220-9.

21. Jiang, X., Shen, S., Cadwell, C.R., Berens, P., Sinz, F., Ecker, A.S., Patel, S., and Tolias, A.S. (2015). Principles of connectivity among morphologically defined cell types in adult neocortex. Science *350*, aac9462. https://doi.org/10.1126/science.aac9462.

22. Perin, R., Berger, T.K., and Markram, H. (2011). A synaptic organizing principle for cortical neuronal groups. Proc. Natl. Acad. Sci. USA *108*, 5419–5424. https://doi.org/10.1073/pnas.1016051108.

23. Blümcke, I., Thom, M., Aronica, E., Armstrong, D.D., Bartolomei, F., Bernasconi, A., Bernasconi, N., Bien, C.G., Cendes, F., Coras, R., et al. (2013). International consensus classification of hippocampal sclerosis in temporal lobe epilepsy: a Task Force report from the ILAE Commission on Diagnostic Methods. Epilepsia *54*, 1315–1329. https://doi.org/10.1111/epi.12220.

24. Kanari, L., Shi, Y., Arnaudon, A., Barros-Zulaica, N., Benavides-Piccione, R., Coggan, J.S., DeFelipe, J., Hess, K., Mansvelder, H.D., Mertens, E.J., et al. (2024). Of mice and men: topologically complex dendrites assemble uniquely human networks. Preprint at bioRxiv. https://doi.org/10.1101/2023.09.11.557170.

25. Peng, Y., Bjelde, A., Aceituno, P.V., Mittermaier, F.X., Planert, H., Grosser, S., Onken, J., Faust, K., Kalbhenn, T., Simon, M., et al. (2024). Directed and acyclic synaptic connectivity in the human layer 2–3 cortical microcircuit. Science *384*, 338–343. https://doi.org/10.1126/science.adg8828.

26. Miles, R., and Wong, R.K.S. (1986). Excitatory synaptic interactions between CA3 neurones in the guinea-pig hippocampus. J. Physiol. *373*, 397–418. https://doi.org/10.1113/jphysiol.1986.sp016055.

27. Sammons, R.P., Vezir, M., Moreno-Velasquez, L., Cano, G., Orlando, M., Sievers, M., Grasso, E., Metodieva, V.D., Kempter, R., Schmidt, H., et al. (2024). Structure and function of the hippocampal CA3 module. Proc. Natl. Acad. Sci. USA *121*, e2312281120. https://doi.org/10.1073/pnas.2312281120.

28. Hunt, S., Leibner, Y., Mertens, E.J., Barros-Zulaica, N., Kanari, L., Heistek, T.S., Karnani, M.M., Aardse, R., Wilbers, R., Heyer, D.B., et al. (2023). Strong and reliable synaptic communication between pyramidal neurons in adult human cerebral cortex. Cereb. Cortex *33*, 2857–2878. https://doi.org/10.1093/cercor/bhac246.

29. Erdős, P., and Rényi, A. (1959). On random graphs. I. Publ. Math. Debrecen *6*, 290–297. https://doi.org/10.5486/PMD.1959.6.3-4.12.

30. Attili, S.M., Moradi, K., Wheeler, D.W., and Ascoli, G.A. (2022). Quantification of neuron types in the rodent hippocampal formation by data mining and numerical optimization. Eur. J. Neurosci. *55*, 1724–1741. https://doi.org/10.1111/ejn.15639.

31. Boss, B.D., Turlejski, K., Stanfield, B.B., and Cowan, W.M. (1987). On the numbers of neurons in fields CA1 and CA3 of the hippocampus of Sprague-Dawley and Wistar rats. Brain Res. *406*, 280–287. https://doi.org/10.1016/0006-8993(87)90793-1.

32. González-Arnay, E., Pérez-Santos, I., Jiménez-Sánchez, L., Cid, E., Gal, B., de la Prida, L.M., and Cavada, C. (2024). Immunohistochemical field parcellation of the human hippocampus along its antero-posterior axis. Brain Struct. Funct. *229*, 359–385. https://doi.org/10.1007/s00429-023-02725-9.

33. West, M.J., and Gundersen, H.J. (1990). Unbiased stereological estimation of the number of neurons in the human hippocampus. J. Comp. Neurol. *296*, 1–22. https://doi.org/10.1002/cne.902960102.

34. West, M.J. (1993). Regionally specific loss of neurons in the aging human hippocampus. Neurobiol. Aging *14*, 287–293. https://doi.org/10.1016/0197-4580(93)90113-P.

35. Simić, G., Kostović, I., Winblad, B., and Bogdanović, N. (1997). Volume and number of neurons of the human hippocampal formation in normal aging and Alzheimer's disease. J. Comp. Neurol. *379*, 482–494. https://pubmed.ncbi.nlm.nih.gov/9067838/.

36. Seress, L. (1988). Interspecies comparison of the hippocampal formation shows increased emphasis on the regio superior in the Ammon's horn of the human brain. J. Hirnforsch. *29*, 335–340. https://europepmc.org/article/MED/3418118.

37. Benavides-Piccione, R., Regalado-Reyes, M., Fernaud-Espinosa, I., Kastanauskaite, A., Tapia-González, S., León-Espinosa, G., Rojo, C., Insausti, R., Segev, I., and DeFelipe, J. (2020). Differential structure of hippocampal CA1 pyramidal neurons in the human and mouse. Cereb. Cortex *30*, 730–752. https://doi.org/10.1093/cercor/bhz122.

38. Wang, S.S.-H., Ambrosini, A.E., and Wittenberg, G.M. (2016). Evolution and scaling of dendrites. In Dendrites, G. Stuart, N. Spruston, and M. Häusser, eds. (Oxford University Press), pp. 47–76. https://doi.org/10.1093/acprof:oso/9780198745273.003.0002.

39. Tillberg P.W., Chen F., Piatkevich K.D., Zhao Y., Yu C.-C. (Jay), English B.P., Gao L., Martorell A., Suk H.-J., Yoshida F., et al. Protein-retention expansion microscopy of cells and tissues labeled using standard fluorescent proteins and antibodies. Nat. Biotechnol. 2016;34:987–992. https://doi.org/10.1038/nbt.3625.

40. Loomba, S., Straehle, J., Gangadharan, V., Heike, N., Khalifa, A., Motta, A., Ju, N., Sievers, M., Gempt, J., Meyer, H.S., et al. (2022). Connectomic comparison of mouse and human cortex. Science *377*, eabo0924. https://doi.org/10.1126/science.abo0924.

41. Blackstad, T.W. (1956). Commissural connections of the hippocampal region in the rat, with special reference to their mode of termination. J. Comp. Neurol. *105*, 417–537. https://doi.org/10.1002/cne.901050305.

42. Qiu, S., Hu, Y., Huang, Y., Gao, T., Wang, X., Wang, D., Ren, B., Shi, X., Chen, Y., Wang, X., et al. (2024). Whole-brain spatial organization of hippocampal single-neuron projectomes. Science *383*, eadj9198. https://doi.org/10.1126/science.adj9198.

43. Ishizuka, N., Weber, J., and Amaral, D.G. (1990). Organization of intrahippocampal projections originating from CA3 pyramidal cells in the rat. J. Comp. Neurol. *295*, 580–623. https://doi.org/10.1002/cne.902950407.

44. Kondo, H., Lavenex, P., and Amaral, D.G. (2009). Intrinsic connections of the macaque monkey hippocampal formation: II. CA3 connections. J. Comp. Neurol. *515*, 349–377. https://doi.org/10.1002/cne.22056.

45. Witter, M.P. (2007). Intrinsic and extrinsic wiring of CA3: indications for connectional heterogeneity. Learn. Mem. *14*, 705–713. https://doi.org/10.1101/lm.725207.

46. Wittner, L., Henze, D.A., Záborszky, L., and Buzsáki, G. (2007). Three-dimensional reconstruction of the axon arbor of a CA3 pyramidal cell recorded and filled in vivo. Brain Struct. Funct. *212*, 75–83. https://doi.org/10.1007/s00429-007-0148-y.

47. Mountcastle, V.B. (1997). The columnar organization of the neocortex. Brain *120*, 701–722. https://doi.org/10.1093/brain/120.4.701.

48. Douglas, R.J., and Martin, K.A.C. (2004). Neuronal circuits of the neocortex. Annu. Rev. Neurosci. *27*, 419–451. https://doi.org/10.1146/annurev.neuro.27.070203.144152.

49. Jouhanneau, J.-S., Kremkow, J., and Poulet, J.F.A. (2018). Single synaptic inputs drive high-precision action potentials in parvalbumin expressing GABA-ergic cortical neurons in vivo. Nat. Commun. *9*, 1540. https://doi.org/10.1038/s41467-018-03995-2.

50. Hopfield, J.J. (1982). Neural networks and physical systems with emergent collective computational abilities. Proc. Natl. Acad. Sci. USA *79*, 2554–2558. https://doi.org/10.1073/pnas.79.8.2554.

51. Bennett, M.R., Gibson, W.G., and Robinson, J. (1994). Dynamics of the CA3 pyramidal neuron autoassociative memory network in the hippocampus. Philos. Trans. R. Soc. Lond. B Biol. Sci. *343*, 167–187. https://doi.org/10.1098/rstb.1994.0019.

52. Papamakarios, G., and Murray, I. (2016). Fast ε-free inference of simulation models with Bayesian conditional density estimation. Adv. Neural Inf. Process. Syst. *29*, 1028–1036. https://proceedings.neurips.cc/paper/2016/file/6aca97005c68f1206823815f66102863-Paper.pdf.

53. Gonçalves, P.J., Lueckmann, J.-M., Deistler, M., Nonnenmacher, M., Öcal, K., Bassetto, G., Chintaluri, C., Podlaski, W.F., Haddad, S.A., Vogels, T.P., et al. (2020). Training deep neural density estimators to identify mechanistic models of neural dynamics. eLife *9*, e56261. https://doi.org/10.7554/eLife.56261.

54. Pelkey, K.A., Vargish, G.A., Pellegrini, L.V., Calvigioni, D., Chapeton, J., Yuan, X., Hunt, S., Cummins, A.C., Eldridge, M.A.G., Pickel, J., et al. (2023). Evolutionary conservation of hippocampal mossy fiber synapse properties. Neuron *111*, 3802–3818.e5. https://doi.org/10.1016/j.neuron.2023.09.005.

55. Amrein, I., Slomianka, L., and Lipp, H.-P. (2004). Granule cell number, cell death and cell proliferation in the dentate gyrus of wild-living rodents. Eur. J. Neurosci. *20*, 3342–3350. https://doi.org/10.1111/j.1460-9568.2004.03795.x.

56. Ihunwo, A.O., and Schliebs, R. (2010). Cell proliferation and total granule cell number in dentate gyrus of transgenic Tg2576 mouse. Acta Neurobiol. Exp. *70*, 362–369. https://doi.org/10.55782/ane-2010-1808.

57. Lim, C., Blume, H.W., Madsen, J.R., and Saper, C.B. (1997). Connections of the hippocampal formation in humans: I. The mossy fiber pathway. J. Comp. Neurol. *385*, 325–351. https://onlinelibrary.wiley.com/doi/10.1002/(SICI)1096-9861(19970901)385:3%3C325::AID-CNE1%3E3.0.CO;2-5.

58. Lauer, M., and Senitz, D. (2006). Dendritic excrescences seem to characterize hippocampal CA3 pyramidal neurons in humans. J. Neural Transm. (Vienna) *113*, 1469–1475. https://doi.org/10.1007/s00702-005-0428-8.

59. Lu, D., He, L., Xiang, W., Ai, W.-M., Cao, Y., Wang, X.-S., Pan, A., Luo, X.-G., Li, Z., and Yan, X.-X. (2013). Somal and dendritic development of human CA3 pyramidal neurons from midgestation to middle childhood: a quantitative Golgi study. Anat. Rec. *296*, 123–132. https://doi.org/10.1002/ar.22616.

60. Tavakoli, M.R., Lyudchik, J., Januszewski, M., Vistunou, V., Agudelo, N., Vorlaufer, J., Sommer, C., Kreuzinger, C., Oliveira, B., Cenameri, A., et al. (2024). Light-microscopy based dense connectomic reconstruction of mammalian brain tissue. Preprint at bioRxiv. https://doi.org/10.1101/2024.03.01.582884.

61. Amaral, D.G., Ishizuka, N., and Claiborne, B. (1990). Neurons, numbers and the hippocampal network. Prog. Brain Res. *83*, 1–11. https://doi.org/10.1016/s0079-6123(08)61237-6.

62. Rolls, E.T. (2018). The storage and recall of memories in the hippocampo-cortical system. Cell Tissue Res. *373*, 577–604. https://doi.org/10.1007/s00441-017-2744-3.

63. Dietrich, D., Clusmann, H., Kral, T., Steinhäuser, C., Blümcke, I., Heinemann, U., and Schramm, J. (1999). Two electrophysiologically distinct types of granule cells in epileptic human hippocampus. Neuroscience *90*, 1197–1206. https://doi.org/10.1016/S0306-4522(98)00574-0.

64. Cohen, I., Navarro, V., Clemenceau, S., Baulac, M., and Miles, R. (2002). On the origin of interictal activity in human temporal lobe epilepsy in vitro. Science *298*, 1418–1421. https://doi.org/10.1126/science.1076510.

65. Wittner, L., Huberfeld, G., Clémenceau, S., Erőss, L., Dezamis, E., Entz, L., Ulbert, I., Baulac, M., Freund, T.F., Maglóczky, Z., et al. (2009). The epileptic human hippocampal cornu ammonis 2 region generates spontaneous interictal-like activity in vitro. Brain *132*, 3032–3046. https://doi.org/10.1093/brain/awp238.

66. Hamilton, T.J., Wheatley, B.M., Sinclair, D.B., Bachmann, M., Larkum, M.E., and Colmers, W.F. (2010). Dopamine modulates synaptic plasticity in dendrites of rat and human dentate granule cells. Proc. Natl. Acad. Sci. USA *107*, 18185–18190. https://doi.org/10.1073/pnas.1011558107.

67. Allen, C., and Stevens, C.F. (1994). An evaluation of causes for unreliability of synaptic transmission. Proc. Natl. Acad. Sci. USA *91*, 10380–10383. https://doi.org/10.1073/pnas.91.22.10380.

68. Marr, D. (1971). Simple memory: a theory for archicortex. Philos. Trans. R. Soc. Lond. B Biol. Sci. *262*, 23–81. https://doi.org/10.1098/rstb.1971.0078.

69. Holler, S., Köstinger, G., Martin, K.A.C., Schuhknecht, G.F.P., and Stratford, K.J. (2021). Structure and function of a neocortical synapse. Nature *591*, 111–116. https://doi.org/10.1038/s41586-020-03134-2.

70. Sorra, K.E., and Harris, K.M. (1993). Occurrence and three-dimensional structure of multiple synapses between individual radiatum axons and their target pyramidal cells in hippocampal area CA1. J. Neurosci. *13*, 3736–3748. https://doi.org/10.1523/JNEUROSCI.13-09-03736.1993.

71. Bourne, J.N., Chirillo, M.A., and Harris, K.M. (2013). Presynaptic ultrastructural plasticity along CA3→CA1 axons during LTP in mature hippocampus. J. Comp. Neurol. *521*, 3898–3912. https://doi.org/10.1002/cne.23384.

72. Rigby, M., Grillo, F.W., Compans, B., Neves, G., Gallinaro, J., Nashashibi, S., Horton, S., Pereira Machado, P.M., Carbajal, M.A., Vizcay-Barrena, G., et al. (2023). Multi-synaptic boutons are a feature of CA1 hippocampal connections in the stratum oriens. Cell Rep. *42*, 112397. https://doi.org/10.1016/j.celrep.2023.112397.

73. Kullmann, D.M. (2003). Silent synapses: what are they telling us about long-term potentiation? Philos. Trans. R. Soc. Lond. B Biol. Sci. *358*, 727–733. https://doi.org/10.1098/rstb.2002.1229.

74. Vardalaki, D., Chung, K., and Harnett, M.T. (2022). Filopodia are a structural substrate for silent synapses in adult neocortex. Nature *612*, 323–327. https://doi.org/10.1038/s41586-022-05483-6.

75. Watson, J.F., Vargas-Barroso, V., and Jonas, P. (2024). Cell-specific wiring routes information flow through hippocampal. Preprint at bioRxiv. https://doi.org/10.1101/2024.06.24.600436.

76. Slomianka, L., Amrein, I., Knuesel, I., Sørensen, J.C., and Wolfer, D.P. (2011). Hippocampal pyramidal cells: the reemergence of cortical lamination. Brain Struct. Funct. *216*, 301–317. https://doi.org/10.1007/s00429-011-0322-0.

77. Cembrowski, M.S., and Spruston, N. (2019). Heterogeneity within classical cell types is the rule: lessons from hippocampal pyramidal neurons.

Nat. Rev. Neurosci. *20*, 193–204. https://doi.org/10.1038/s41583-019-0125-5.

78. Hunt, D.L., Linaro, D., Si, B., Romani, S., and Spruston, N. (2018). A novel pyramidal cell type promotes sharp-wave synchronization in the hippocampus. Nat. Neurosci. *21*, 985–995. https://doi.org/10.1038/s41593-018-0172-7.

79. Magó, Á., Kis, N., Lükő, B., and Makara, J.K. (2021). Distinct dendritic Ca^{2+} spike forms produce opposing input-output transformations in rat CA3 pyramidal cells. eLife *10*, e74493. https://doi.org/10.7554/eLife.74493.

80. Scheibel, M.E., Davies, T.L., Lindsay, R.D., and Scheibel, A.B. (1974). Basilar dendrite bundles of giant pyramidal cells. Exp. Neurol. *42*, 307–319. https://doi.org/10.1016/0014-4886(74)90028-4.

81. Guzman, S.J., Schlögl, A., and Schmidt-Hieber, C. (2014). Stimfit: quantifying electrophysiological data with Python. Front. Neuroinform. *8*, 16. https://doi.org/10.3389/fninf.2014.00016.

82. Feng, L., Zhao, T., and Kim, J. (2015). neuTube 1.0: A new design for efficient neuron reconstruction software based on the SWC format. eNeuro *2*, 0049–14.2014. https://doi.org/10.1523/ENEURO.0049-14.2014.

83. Schindelin, J., Arganda-Carreras, I., Frise, E., Kaynig, V., Longair, M., Pietzsch, T., Preibisch, S., Rueden, C., Saalfeld, S., Schmid, B., et al. (2012). Fiji – an open source platform for biological image analysis. Nat. Methods *9*, 676–682. https://doi.org/10.1038/nmeth.2019.

84. Berg, S., Kutra, D., Kroeger, T., Straehle, C.N., Kausler, B.X., Haubold, C., Schiegg, M., Ales, J., Beier, T., Rudy, M., et al. (2019). ilastik: interactive machine learning for (bio)image analysis. Nat. Methods *16*, 1226–1232. https://doi.org/10.1038/s41592-019-0582-9.

85. Berger, D.R., Seung, H.S., and Lichtman, J.W. (2018). VAST (Volume Annotation and Segmentation Tool): efficient manual and semi-automatic labeling of large 3D image stacks. Front. Neural Circuits *12*, 88. https://doi.org/10.3389/fncir.2018.00088.

86. Tejero-Cantero, A., Boelts, J., Deistler, M., Lueckmann, J.-M., Durkan, C., Gonçalves, P.J., Greenberg, D.S., and Macke, J.H. (2020). sbi: A toolkit for simulation-based inference. J. Open Source Softw. *5*, 2505. https://doi.org/10.21105/joss.02505.

87. Najm, I., Lal, D., Alonso Vanegas, M., Cendes, F., Lopes-Cendes, I., Palmini, A., Paglioli, E., Sarnat, H.B., Walsh, C.A., Wiebe, S., et al. (2022). The ILAE consensus classification of focal cortical dysplasia: an update proposed by an ad hoc task force of the ILAE diagnostic methods commission. Epilepsia *63*, 1899–1919. https://doi.org/10.1111/epi.17301.

88. Bischofberger, J., Engel, D., Li, L., Geiger, J.R.P., and Jonas, P. (2006). Patch-clamp recording from mossy fiber terminals in hippocampal slices. Nat. Protoc. *1*, 2075–2081. https://doi.org/10.1038/nprot.2006.312.

89. Jones, E.G., Hendry, S.H.C., Liu, X.B., Hodgins, S., Potkin, S.G., and Tourtellotte, W.W. (1992). A method for fixation of previously fresh-frozen human adult and fetal brains that preserves histological quality and immunoreactivity. J. Neurosci. Methods *44*, 133–144. https://doi.org/10.1016/0165-0270(92)90006-Y.

90. Jonas, P., Major, G., and Sakmann, B. (1993). Quantal components of unitary EPSCs at the mossy fibre synapse on CA3 pyramidal cells of rat hippocampus. J. Physiol. *472*, 615–663. https://doi.org/10.1113/jphysiol.1993.sp019965.

91. Clements, J.D., and Bekkers, J.M. (1997). Detection of spontaneous synaptic events with an optimally scaled template. Biophys. J. *73*, 220–229. https://doi.org/10.1016/S0006-3495(97)78062-7.

92. Tainaka, K., Kubota, S.I., Suyama, T.Q., Susaki, E.A., Perrin, D., Ukai-Tadenuma, M., Ukai, H., and Ueda, H.R. (2014). Whole-body imaging with single-cell resolution by tissue decolorization. Cell *159*, 911–924. https://doi.org/10.1016/j.cell.2014.10.034.

93. Wheeler, D.W., White, C.M., Rees, C.L., Komendantov, A.O., Hamilton, D.J., and Ascoli, G.A. (2015). Hippocampome.org: a knowledge base of neuron types in the rodent hippocampus. eLife *4*, e09960. https://doi.org/10.7554/eLife.09960.

94. Gibson, W.G., and Robinson, J. (1992). Statistical analysis of the dynamics of a sparse associative memory. Neural Netw. *5*, 645–661. https://doi.org/10.1016/S0893-6080(05)80042-5.

95. Confavreux, B., Ramesh, P., Gonçalves, P.J., Macke, J.H., and Vogels, T.P. (2024). Meta-learning families of plasticity rules in recurrent spiking networks using simulation-based inference. Adv. Neural Inf. Process. Syst. *36*, 13545–13558. https://proceedings.neurips.cc/paper_files/paper/2023/file/2bdc2267c3d7d01523e2e17ac0a754f3-Paper-Conference.pdf.

96. Gray, H. (1918). Anatomy of the Human Body (Lea & Febiger). https://books.google.com/books/about/Anatomy_of_the_Human_Body.html?id=uaQMAAAAYAAJ.

STAR★METHODS

KEY RESOURCES TABLE

REAGENT or RESOURCE	SOURCE	IDENTIFIER
Antibodies		
Rabbit polyclonal anti-NeuN	Thermo Fisher Scientific	RRID:AB_2554049
Goat anti-rabbit AF488	Thermo Fisher Scientific	RRID:AB_2576217
Biotinylated anti-streptavidin	Vector Laboratories	RRID:AB_2336221
Biological samples		
Human patient brain samples	Med. Uni. Wien (MUW)	https://neurochirurgie.meduniwien.ac.at/
Human postmortem tissue	NABCA biobank	http://nabca.eu/
Chemicals, peptides, and recombinant proteins		
Biocytin	Invitrogen	#B1592
Paraformaldehyde (PFA)	TAAB	P001/2
Paraformaldehyde (PFA)	Sigma-Aldrich	158127
AF647 conjugated streptavidin	Invitrogen	S32357
Mowiol 4-88	Carl Roth	713.2
Vectastain Elite ABC HRP-Kit	Vector Laboratories	PK-6100
3,3′-diaminobenzidine -tetrahydrochloride hydrate (DAB)	Sigma-Aldrich	D5637-5G
Acryloyl-X, SE (6-((acryloyl)amino)hexanoic acid, succinimidyl ester)	Thermo Fisher Scientific	A20770
Sodium acrylate	AK Scientific	R624
Acrylamide (AA)	Sigma-Aldrich	A9099
Methylene bisacrylamide (BIS)	Sigma-Aldrich	M7279
Ammonium persulfate (APS)	Sigma-Aldrich	A3678
N,N,N′-Tetramethylethylenediamine (TEMED)	Sigma-Aldrich	T9281
Proteinase K	Sigma-Aldrich	P4850-1ML
4-Hydroxy-2,2,6,6-tetramethylpiperidine 1-oxyl (TEMPO)	Sigma-Aldrich	176141
Glycerol triglycidyl ether (TGE)	Polysciences Europe GmbH	09221
Poly-L-Lysine Hydrochloride	Sigma-Aldrich	S5881
NHS-Atto 488	Atto-Tec	AD488–31
NHS-AF488	Jena Bioscience	APC-002-1
Experimental models: Organisms/strains		
Mouse: C57BL/6J	The Jackson Laboratory	RRID: IMSR_JAX000664
Rat: Wistar	Charles River	RRID: RDG_13508588
Software and algorithms		
Stimfit v.0.15.8	Guzman et al.[81]	https://github.com/neurodroid/stimfit
Signal v.6.0	CED	N/A
MATLAB R2022b	Mathworks	https://de.mathworks.com/products/matlab.html
Imaris Stitcher Software	Oxford Instruments	https://imaris.oxinst.com/products/imaris-stitcher
Imaris 9	Oxford Instruments	https://imaris.oxinst.com/
Neutube analysis software	Feng et al.[82]	https://neutracing.com/
Neurolucida	MBF Bioscience	https://www.mbfbioscience.com/products/neurolucida/
FIJI/Image J	Schindelin et al.[83]	https://fiji.sc/
ILASTIK	Berg et al.[84]	https://www.ilastik.org/
VAST lite v1.4.0	Berger et al.[85]	https://lichtman.rc.fas.harvard.edu/vast/
Python 3.7.12	Python Software Foundation	https://www.python.org/

Continued		
REAGENT or RESOURCE	SOURCE	IDENTIFIER
Sbi 0.22	Tejero-Cantero et al.[86]	https://sbi-dev.github.io/sbi/
GraphPad Prism v.10.2.2	GraphPad	https://www.graphpad.com/features
Other		
Borosilicate glass tubing	Hilgenberg	1807542

EXPERIMENTAL MODEL AND STUDY PARTICIPANT DETAILS

Human patient tissue samples
Human tissue samples were obtained with informed patient consent from 17 individuals with TLE. This work was approved by the Ethics Committee of the Medical University Vienna (MUW) (EK Nr: 2271/2021). Neuropathological changes ranged from substantially altered temporo-mesial regions in patients with hippocampal sclerosis to unaffected temporo-mesial structures in a cavernoma patient. Tissue samples were used in a pseudonymised manner, such that patient identity was only available to clinicians. Samples included both hippocampal hemispheres and patients of both sexes, with an age range of 15 to 51 years, all of White European ethnicity (Table S1).

Human postmortem tissue samples
Three blocks (each approximately 1 cm^3) of postmortem tissue were acquired from the Normal Ageing Brain Collection Amsterdam (NABCA) biobank (Project agreement METC: 2023.0733; ISTA Ethics committee application: 2023-03). Samples of hippocampal body from the left hemisphere had been taken from donors of both sexes with no known neurological conditions, aged 77, 84, and 63 at death. The postmortem delay time to autopsy start was 4.5, 5, and 6 h respectively. Samples were snap frozen after dissection and stored at $-80°C$ until use.

Animals
All procedures were performed in strict accordance with institutional, national, and European guidelines for animal experimentation, approved by the Bundesministerium für Wissenschaft, Forschung und Wirtschaft of Austria (BMBWF-V/Sb 2021-0.547.215 and 2020-0.648.587). Wild-type C57BL/6J mice (RRID:IMSR_JAX:000664) and wild-type Wistar rats (RRID:RGD_13508588) of both sexes were used at postnatal (P) day 20–30 unless otherwise stated (median age: P23). All animals were housed with *ad libitum* access to food and water, with constant temperature and humidity of 22°C and 50–60%, respectively, under a 12-hr light-dark cycle, and used for experiments during the light phase.

METHOD DETAILS

Human patient sample acquisition
All patients underwent presurgical MRI, allowing analysis of the likely degree of hippocampal sclerosis. Targeted resection of neocortical and hippocampal tissue was performed unilaterally. The hippocampus and parahippocampal gyrus (PHG) were surgically harvested in a maximally careful manner, with the goal to avoid any mechanical or hypoxic damage to the tissue. The applied surgical technique of anteromesial temporal lobe resection (AMTLR) allowed us to achieve both of these goals. The temporal pole was resected first, without touching the hippocampus and PHG. Secondly, the temporal horn of the ventricle was opened and the lateral neocortical tissue was resected. Consecutively, the hippocampus/PHG was prepared in a way that the vascular supply was disconnected just before removal, so that an "en bloc" specimen was transferred immediately to the transport solution. A substantial portion of resected tissue was sent to the neuropathological laboratory (Division of Neuropathology and Neurochemistry, Department of Neurology, Medical University of Vienna, MUW) for complete histological assessment, neuropathological diagnosis, and sub-classification according to international league against epilepsy (ILAE) sclerosis standards[23,87] (see Table S1 for details). An MRI image was provided (Figure 1B) with informed consent from the patient and the Department of Biomedical Imaging and Image-guided Therapy, Division of Neuroradiology and Musculoskeletal Radiology of MUW.

Preparation of human tissue slices
Tissue blocks of human hippocampus (typically ~1 cm^3) and cortex were removed from the brain, and immediately submerged in ice-cold high-sucrose artificial cerebrospinal fluid (aCSF, containing 64 mM NaCl, 25 mM NaHCO$_3$, 2.5 mM KCl, 1.25 mM NaH$_2$PO$_4$, 10 mM D-glucose, 120 mM sucrose, 7 mM MgCl$_2$, and 0.5 mM CaCl$_2$; osmolarity ~334 mOsm) equilibrated by bubbling with 95% O$_2$ and 5% CO$_2$ gas mixture (carbogen). Samples were typically from the anterior hippocampus, comprising the hippocampal body bordering and occasionally including part of the uncus. Samples were transported to the laboratory on ice with continuous carbogen bubbling. The time between departure from the surgery room to arrival in the lab for slice preparation was 37–50 min

(mean: 43 min). Hippocampal tissue blocks were trimmed to remove the PHG, and to form a gluing face perpendicular to the longitudinal axis of the hippocampus, allowing best preservation of dendritic integrity. Tissue blocks were glued to the specimen plate of a Leica VT 1200 vibratome (Leica Microsystems) with liquid superglue (UHU), and submerged in a partially frozen 'slush' of ice-cold high-sucrose aCSF with supplemental carbogen bubbling. 350-μm-thick acute slices were cut (blade advance velocity 0.04–0.05 mm s^{-1}, oscillation amplitude 1.2 mm), before recovery at 35°C in high-sucrose aCSF for 30–45 min. Slices were recovered and recorded with their cut face downwards. After recovery, slices were maintained in bubbled high-sucrose aCSF at room temperature (RT; 20–22°C) until recording. The solution in the maintenance chamber was exchanged every 2–4 h to maintain slice health. Cortical tissue blocks were cut similarly, with macroscopic trimming to best preserve the dendritic tree of cortical PNs. Slices were typically used for up to 16 h after sectioning.

Rodent acute slice preparation

Animals were sacrificed by decapitation under isoflurane anesthesia. Brains were extracted rapidly in ice-cold high-sucrose aCSF (see above) equilibrated with carbogen. Hemispheres were separated by a single sagittal cut using a scalpel blade. Acute slices were cut using the 'magic-cut' quasi-transverse preparation, whereby the dorsal surface of the brain was cut parallel to the brain surface[88] and glued to the specimen plate of a Leica VT 1200 vibratome using liquid superglue (UHU). Slices therefore originated from mid to ventral hippocampus. Tissue blocks were cut as per human tissue, in partially frozen high-sucrose aCSF, and cut into 350-μm-thick slices. Slices were then transferred to a recovery chamber containing high-sucrose aCSF at 35°C for 30–45 min before maintenance in this solution at RT until recording.

Postmortem tissue handling

Postmortem samples were fixed from frozen material following Jones et al.[89] Frozen samples were immersed in a fixation solution containing 4% (w/v) paraformaldehyde (PFA; TAAB Laboratories), 20% (w/v) sucrose, 20% (v/v) ethanol, 20% (v/v) ethylene glycol, and 10% (v/v) glycerol in 0.1 M phosphate buffer (PB; 0.1 M NaH$_2$PO$_4$ and 0.1 M Na$_2$HPO$_4$, Merck; titrated to pH 7.35) that had been pre-chilled on dry ice. Samples were then incubated at −55°C for 12–24 h, warmed to −20°C across 3.5 h, held at −20°C for 12 h, and warmed to 4°C over 2.4 h, using a Leica AFS2 freeze-substitution device, with manual agitation at periodic intervals. Samples were then post-fixed overnight at 4°C with 4% PFA in 0.1 M PB, and sectioned to 350-μm slices using a Leica VT 1200 vibratome. Control mouse tissue for spine density measurement was processed similarly, by submerging whole, freshly dissected brains in liquid N$_2$ and proceeding with freeze-substitution as per human samples. Downstream handling for immunostaining and LICONN imaging was performed as described below.

Electrophysiology

Slices were transferred to the recording chamber and continuously perfused under gravity flow with recording aCSF (containing 125 mM NaCl, 25 mM NaHCO$_3$, 2.5 mM KCl, 1.25 mM NaH$_2$PO$_4$, 25 mM D-glucose, 2 mM CaCl$_2$, and 1 mM MgCl$_2$, osmolarity ~317 mOsm) continuously bubbled with carbogen. Slices were held in place with a platinum harp with nylon threads to prevent tissue movement during recordings. Patch-clamp recording pipettes were pulled from thick-walled borosilicate glass tubing (Hilgenberg, 2 mm OD, 1 mm ID, 1807542), and filled with intracellular solution (containing 135 mM K gluconate, 20 mM KCl, 0.1 mM EGTA, 2 mM MgCl$_2$, 2 mM Na$_2$ATP, 0.3 mM NaGTP, and 10 mM HEPES, adjusted to pH 7.28 with KOH; osmolarity ~302 mOsm, with 0.2% (w/v) biocytin). Micropipettes had open-tip resistances of 2–6 MΩ when filled with internal solution, and were positioned manually using eight Junior 20ZR or LN mini 25 micromanipulators (Luigs and Neumann). Neurons were targeted using IR-DIC videomicroscopy based on their soma location in the CA3 pyramidal cell layer. All cells were confirmed to be CA3 PNs based on firing properties and post-hoc morphological analysis. Human CA3 PNs were predominantly recorded from the proximal region of CA3 (closest to the dentate gyrus), while rodent CA3 PNs were recorded from across the proximal-distal axis. Electrical signals were recorded using four Multiclamp 700B amplifiers (Molecular Devices), low-pass filtered at 6–10 kHz with built-in Bessel filters, and digitized at 20 kHz with Power 1401 data acquisition interfaces (Cambridge Electronic Design). Protocols were generated and applied using Signal 6.0 software (CED). Pipette offset and capacitance were measured and accounted for during all recordings. During current-clamp recordings, pipette capacitance was ~70% compensated in all cases, and series resistance compensation was applied as appropriate. All recordings were performed at RT.

Neuronal firing properties were assessed by injection of 1-s hyperpolarizing or depolarizing currents in 50 pA steps. Synaptic connectivity was tested by eliciting APs in each recorded neuron in current-clamp mode in turn, while recording responses from all other neurons in either current- or voltage-clamp configurations. APs were elicited by brief current injection (2–5 ms) at a minimal level to reliably evoke single spikes (typically 1–2 nA in rodents, and 2–4 nA in human cells). Connectivity was routinely tested by stimulation with 5 APs at 20 Hz, repeated at least 40 times. Monosynaptic connections were typically identified by reliable appearance of synaptic responses in the average trace, and short latency (< 4 ms) and minimal temporal jitter (< 0.5 ms) of individual sweeps. A subset of human synapses showed longer latencies but low jitter, and were therefore considered putative monosynaptic connections (see Figure S3C). Electrical coupling was tested by injection of a 50-pA hyperpolarizing current for 250 ms to the presynaptic cell, and monitoring responses in all other cells. No electrical coupling was observed between CA3 PNs in any species. After recordings, pipettes were slowly retracted from the cell somata to form outside-out patches to ensure retention of intracellular biocytin for post-hoc staining. The quality of patch formation and physical location of recorded cells in the tissue slice was documented for later

cell identification in stained tissue. Recorded traces were analyzed using Stimfit (version v0.15.8;[81]) or custom Matlab scripts. Cells with a membrane potential above −50 mV or requiring current injection to maintain membrane potential (V_m) below −50 mV were excluded from analysis of passive and active properties. Resting membrane potential was measured as the median V_m without current injection, input resistance was calculated from −100, −50 and +50 pA injections, and apparent membrane time constant was measured as a monoexponential fit of the 'off step' of hyperpolarizing current injections. The AP threshold criterion was set as dV/dt = 20 V s^{-1}, and half-duration was measured from resting membrane potential. Maximum frequency was calculated from the shortest inter-spike-interval (ISI) between two spikes at a given current injection. Spike-frequency adaptation was measured from the first sweep with at least five APs calculated by dividing the mean of the first two ISIs by the mean of the last two ISIs. Therefore, a value of 1 represents non-adapting spike frequencies, and values closer to 0 are more adapting. All voltage-clamp recordings were performed with a holding potential of −70 mV. sPSCs were detected using a template based analysis (minidet.m, Biosig toolbox, http://biosig.sf.net/; see Jonas et al.[90] and Clements and Bekkers[91]).

Synaptic successes were defined sweeps with responses of consistent latency exceeding 2.5 σ (EPSCs) or 3 σ (EPSPs) of baseline noise immediately prior to AP generation (σ denotes standard deviation). Success probabilities refer to the first pulse of 20-Hz train stimulation. CV analysis of EPSPs and EPSCs was performed by measuring peak amplitude variation (SD/mean) from success sweeps. To prevent other sources of variation from compromising this analysis, EPSC CV measurements were performed after manual removal of all sweeps contaminated by sPSCs during the analysis window. EPSP and EPSC 'potency' represent the amplitude of success sweeps excluding failures. EPSP 'response' refers to the total depolarization after successive stimuli of a train, including effects of temporal summation. Synaptic current rise times are between 20–80% of maximal response, while decay kinetics are time constant of a monoexponential fit. Voltage-clamp synaptic responses were only analyzed for pairs with a postsynaptic access resistance of less than 20 MΩ. Mean ± SEM of R_s of synapses presented for EPSC analysis was 12.3 ± 1.5 MΩ (n = 7) for human CA3, 14.6 ± 1.6 MΩ (n = 8) for human neocortical recordings, and 13.8 ± 1.1 MΩ (n = 16) for mouse CA3 synapses. A small number of synapses were excluded from kinetic analysis due to excessive spontaneous activity making analysis unreliable. No correction was made for liquid junction potentials.

Immunohistochemistry

After recording, slices were fixed with 4% (w/v) PFA in 0.1 M PB (0.1 M NaH$_2$PO$_4$ and 0.1 M Na$_2$HPO$_4$, Merck; titrated to pH 7.35) at 4°C and washed in 0.1 M PB after 24 h to terminate the fixation reaction. Slices were blocked and permeabilized by incubation with solution containing 5% normal goat serum (NGS; Biozol ENG9010-10) and 0.4% Triton X-100 (Sigma-Aldrich) in 0.1 M PB for 2–3 h at RT. Alexa Fluor (AF) 647-conjugated streptavidin (1:300 diluted from 2 mg ml^{-1} stock, Invitrogen S32357) was added, and incubated overnight in blocking/permeabilizing solution at RT with gentle shaking. Samples were then washed in 0.1 M PB (3 x 30 min), before incubation with DAPI (4',6-diamidino-2-phenylindole, dilactate, 0.1 µg ml^{-1} final concentration in PB, Invitrogen D3571) in 0.1 M PB for 10–20 min at RT. Recorded slices were cleared by incubation for 10 min at RT in CUBIC solution[92] (50% sucrose, 25% urea, 10% 2,2',2''-nitrilotriethanol, and 0.1% Triton X-100 in MilliQ water; all Sigma-Aldrich: 16104, U5128-500G, 90279-100ml), before mounting on glass slides (Assistant, Karl Hecht Ref:42406020) beneath a #1.5 thickness glass coverslip (VWR 631-0147) in CUBIC solution surrounded by a ring of Mowiol (Mowiol 4-88, Carl Roth, 713,2; made up according to manufacturer protocol with glycerol and tris(hydroxymethyl)aminomethane; Sigma-Aldrich, G-9012 & 252859) to prevent exposure of CUBIC solution to air. Samples were cured for at least 24 h prior to imaging.

If performed, primary antibody staining was included prior to streptavidin addition by overnight incubation of primary antibodies in blocking/permeabilization solution at RT with gentle shaking. Slices were then washed with 0.1 M PB (3 x 30 min) before overnight incubation with both secondary antibodies and conjugated streptavidin. Human slices were routinely stained with anti-NeuN (diluted 1:300 from stock; rabbit anti-NeuN, Thermo Fisher Scientific PA5-37407, RRID:AB_2554049), visualized with AF488-conjugated anti-rabbit secondary antibody (1:300 from stock; goat anti rabbit AF488, Thermo Fisher Scientific A11034, RRID:AB_2576217). Slides were imaged on an ANDOR Dragonfly microscope (Oxford Instruments) equipped with a Zyla 4.2 Megapixel sCMOS camera (2048 x 2048 pixels). Overview images of all human slices were taken using a 10x air objective (Nikon MRD00105, CFI P-Apo 10x, NA 0.45) and coarse (10 µm) z-steps, while cellular morphology was captured using a 20x water-immersion objective (Nikon MRD77200, CFI P-Apochromat 20x, NA 0.95), imaging all observable fluorescently labeled structures. Higher resolution images for analysis of dendritic spines and thorny excrescences were taken using a 40x water-immersion objective (Nikon MRD77410, Apochromat LWD λS 40x, NA 1.15). Tiles were stitched using Imaris Stitcher software (Oxford Instruments). Pinhole discs with 25 or 40 µm hole diameters were used for 10x and 20x, or 40x objective images, respectively.

A subset of rodent samples were imaged using DAB (3,3'-diaminobenzidine-tetrahydrochloride hydrate) staining, where fixation solution contained 2.5% PFA, 1.25% glutaraldehyde (GA; Carl Roth, 4157.1), and 15% (v/v) saturated picric acid solution (Sigma-Aldrich, P6744-1GA) in PB. After washing with PB, samples were treated with hydrogen peroxide (1%, 10 min; Sigma-Aldrich, 95321–100ml), permeabilized with 1% Triton X-100 (in PB) for 1 h, washed again, and transferred to a solution containing 1% avidin-conjugated horseradish peroxidase complex (Vectastain ABC-Elite Standard kit, Vector Laboratories PK-6100) and 1% Triton X-100 for ∼12 h. After rinsing in 0.1 M PB, slices were incubated with a solution containing 0.036% DAB (Sigma-Aldrich, D5637-5G), 0.006% NiCl$_2$ (Sigma-Aldrich, 223387–25G) and 0.008% CoCl$_2$ (Sigma-Aldrich, C8661-25G), and developed by addition of 0.01% hydrogen peroxide. DAB developed slices were mounted in Mowiol and cured for at least 24 h, before visualization using an Olympus BX61 widefield microscope. Recorded cells were visualized using 4, 10, or 20x objectives.

Recorded cells were confirmed to have somata within the structured pyramidal cell layer-forming 'Ammon's horn'. A subset of cells were recorded with somata outside this layer, closer to the GC layer, which were considered CA4 (see Figure S1B). No synaptic connections (90 tested) were observed between CA4 cells. Neuronal densities were measured by manual segmentation of NeuN-stained neurons from image stacks taken using the 40x water immersion objective in the proximal CA3 region of human slices. Presented data are the mean density of three tissue slices per patient, or slices from three different donors for postmortem measurement. Manual segmentation was performed blind to the experimental subgroup (putative sclerotic vs. non-sclerotic).

Morphological analysis

Stitched image stacks of recorded cells were converted to TIFF format for reconstruction using Neutube analysis software.[82] Semi-automated reconstruction with manual correction of all dendritic processes was performed, producing SWC files for cells of interest. Dendritic identity was manually assigned by visual inspection. A subset of cells was reconstructed using Neurolucida manual reconstruction software (MBF Bioscience), which produced equivalent dendritic length parameters, therefore Neutube data was used in all subsequent analysis. SWC files were analyzed using the Fiji[83] SNT plugin, or using custom MATLAB scripts. Restriction of recorded morphologies to *stratum oriens* and *stratum radiatum* lengths was performed by measurement of layer thicknesses from recorded slices or unequivocal layer visualization from slice autofluorescence. Dendritic identity was classified into apical or basal dendrites with either simple spines, thorny excrescences, or no structures by manual inspection. Axon or dendrite processes terminating at the slice surface were marked with a terminal node. Reconstructions were corrected for compression artifacts due to mounting by scaling to slice thickness of 350 μm.

A subset of recorded cells across multiple patients was fully reconstructed for morphological analysis, however all recorded neurons were visualized to determine axon-corrected connectivity. Corrected connectivity considers only neurons with at least 0.5 mm of traceable axon included as possible presynaptic cells, while all recorded neurons were considered possible postsynaptic partners.

Complete dendritic length was estimated by calculation of 'cut length' on a dendrite-by-dendrite basis for each reconstructed cell. For each dendritic node terminating at the slice surface, the dendritic path length to the soma was measured. The estimated 'cut length' was calculated as the mean downstream dendritic length of all uncut dendrites of the recorded neuron beyond the equivalent somatic path length, accounting for both further dendritic branching and apical vs. basal dendrite identity. Thorny dendrites are closer to the soma than CA3-CA3 recurrent input-receiving dendrites and are typically within the recorded slice. Therefore presented data were not corrected for dendritic cutting.

Intersomatic distance was measured as the 3D Euclidean distance between somatic centers. Only multicellular recordings containing synaptic connections were analyzed. Difference in somatic depth was measured as the relative difference in Euclidean distance between somatic centers and the *stratum pyramidale – stratum radiatum* border. Positive values indicate connections from cells closer to this border to cells closer to *stratum oriens*.

Expansion microscopy for spine density measurement

PFA-fixed and AF647-streptavidin stained slices were first imaged as described above before expansion protocol application. This protocol is a modified version of ProExM,[39] applicable to fixed, CUBIC-cleared, and mounted samples, even over one year post-fixation. Mounted slides were incubated overnight in 0.1 M PB at RT to dissolve Mowiol, before using a paintbrush to transfer tissue slices to a multiwell plate for processing. Samples were first anchored by overnight incubation (~16 h) with 0.1 mg ml^{-1} acryloyl-X (ThermoFisher Scientific, A20770) in phosphate-buffered saline (PBS) without Ca^{2+} and Mg^{2+} at 4°C. Slices were then washed for 1 h in PBS before incubation with gel monomer solution for 3–5 h at 4°C. Monomer solution contained 7% sodium acrylate, 20% acrylamide, 0.1% methylene bisacrylamide, 0.05% ammonium persulfate (APS), and 0.05% tetramethylethylenediamine (TEMED) in Milli-Q water. Samples were placed between glass coverslips, separated by a spacer of glass fragments (3 times #1.5 thickness glass) for gelation at 37°C for 3 h in a moist chamber. The sample was trimmed to the region of interest, and tissue digested by proteinase K (Sigma-Aldrich, P4850; 1:100 dilution to 8 units ml^{-1}) treatment overnight at 37°C in 50 mM Tris (pH 8), 1 mM EDTA, 0.5% Triton X-100, and 1 M NaCl. Digestion buffer was removed by repeated washing in PBS at RT while shaking for 3–4 h. Streptavidin signal was amplified by incubation with biotinylated anti-streptavidin antibody (1:200 dilution, Vector Laboratories, VECBA-0500, RRID:AB_2336221) overnight at 4°C while shaking, before washing in PBS and addition of further AF647-conjugated streptavidin (1:300 dilution) for overnight incubation at 4°C while shaking. Slices were expanded immediately prior to imaging by 30-min incubation in MilliQ water, with repeated water exchange, before imaging on an ANDOR Dragonfly spinning disk microscope as above. Expansion factors were calculated by comparison of pre- and post-expansion images and were measured to be 3.9 ± 0.1, 3.9 ± 0.1, and 3.8 ± 0.1 for mouse, rat, and human, respectively (custom code[60]). Spines were either detected using a machine learning algorithm in ilastik[84] and manually corrected using Imaris 9 (Bitplane), or manually segmented using Neutube. The mean dendritic length per neuron sampled for spine density was 297 ± 67 μm, 320 ± 82 μm, and 564 ± 75 μm per mouse, rat, and human neuron, respectively.

Caveats of anatomical connectivity predictions

While dendritic spine density provides a good approximation of synaptic input, several factors add uncertainty to exact quantifications. EM analysis of human neocortex demonstrated an increase in the proportion of excitatory connections onto PN dendritic shafts, from 0.7% (mice) to 12.0% (humans).[40] It is possible that this also occurs in the hippocampus, leaving our input numbers

underestimated by around 10%. In addition, complex innervation arrangements prevent a definitive determination of input number from spine density measurements. Connected neocortical neurons for example, have a mean of 1.6 synaptic contacts per connection,[69] causing an overestimation of presynaptic neuronal input number from spine counts. While connectomic analysis of CA3 is almost non-existent, multi-contact synapses have been suggested.[14] In CA1, which receives CA3 PN axons, spines appear to overwhelmingly receive a single input,[71] and multi-synaptic boutons[72] or axons[70] rarely contact the same cell twice. Finally, a substantial proportion of synapses in the brain may be functionally silent,[73,74] therefore likely causing overestimations of functional connectivity from structural data. Together, spine density is likely to be a good approximation of the number of CA3 presynaptic neurons in the recurrent circuit, but is not a definitive measure of input number.

Expansion microscopy for synapse reconstruction (LICONN)

Mossy fiber connections and sections of spiny CA3 dendrites in human and mouse samples were reconstructed using high-resolution expansion with LICONN technology,[60] with slight adaptations for the human specimens as detailed below, and manual cell shape annotation.

Mouse samples: three wild-type mice (age 8–10 weeks) were anesthetized, first by isoflurane inhalation (1-2 % v/v), then intraperitoneal ketamine/xylazine (80–100 mg kg^{-1} and 10 mg kg^{-1} of body weight respectively), combined with subcutaneous metamizol injection (200 mg kg^{-1}). Under deep anesthesia, animals were transcardially perfused at a flow rate of 7 ml min^{-1} with RT PBS for 2 min followed by 6 min with RT fixative solution containing 4% (w/v) PFA (pH 7.4, Sigma-Aldrich) and 10% acrylamide (AA) in PBS. Brains were removed and postfixed for $\leq$ 12 h at 4°C with gentle agitation in the same fixative solution. Samples were next washed 3 times in 4°C PBS for ∼1 min each with gentle agitation and then sectioned coronally at 50-μm thickness using a Leica VT 1200S vibratome. Sections were quenched in ice-cold PBS containing 100 mM glycine for 6–8 h at 4°C before washing in 4°C PBS. Samples were stored at 4°C in PBS supplemented with 0.015% NaN$_3$ for up to 3 months.

Human samples: human acute tissue slices (350 μm) were fixed immediately after slicing (see *Preparation of human tissue slices*) in RT fixative solution (4% PFA and 10% AA in PBS) for ∼9 h at RT with gentle agitation. Samples were then washed with PBS, quenched in 100 mM glycine-containing PBS for 30 min at RT, before a further wash with PBS for 30 min at RT, all with gentle agitation. Fixed slices could be similarly stored at 4°C in PBS supplemented with 0.015% NaN$_3$ for up to 3 months.

Further handling was according to Tavakoli et al.[60] with adaptations for human tissue as noted. In brief, sections were washed twice for 15–20 min in PBS at RT and twice for 15–20 min in 100 mM sodium bicarbonate in ddH$_2$O (pH 8.0) at RT, before incubation with 0.1% (w/v) TGE and 0.1% (w/v) GMA (mouse sections) or 1% TGE and 1% GMA (human slices) in 100 mM sodium bicarbonate in ddH$_2$O (pH 8.0) for 3 h at 37 °C with gentle agitation in a chemical hood (TGE, glycerol triglycidyl ether; GMA, glycidyl methacrylate). Samples were washed with repeated solution exchange in RT PBS for 1 h.

First expandable hydrogel: the following sample handling steps were performed on an ice-water bath. The 1st hydrogel monomer solution (10% acrylamide, 12.5% sodium acrylate, 0.075% N,N′-methylenebisacrylamide (BIS), all w/v) was initially supplemented with 0.001% TEMPO and then with 0.15% APS and 0.15% TEMED and vortexed. Brain sections were pre-incubated with the hydrogel monomer solution for either 30–45 min (mouse) or 60–70 min (human) with gentle agitation in a 24-well plate. A gelation chamber was assembled as detailed in *Expansion microscopy for spine density measurement*, and gelation was performed for 2 h at 37°C in a humidified chamber.

After gelation, the hydrogel-tissue hybrid was trimmed to the region of interest and transferred to a 5-ml beaker with 2 ml of denaturation buffer (200 mM SDS, 200 mM NaCl, 50 mM Tris-HCl in ddH$_2$O, pH adjusted to 9.0 with NaOH). The beaker was placed in a larger vessel containing pre-heated water and transferred to a water bath at 95°C for either 100 (mouse) or 300 min (human). Samples were expanded in ddH$_2$O, with water exchange every 20 min until gel size increased no further. Unreacted crosslinker was neutralized by incubation with 0.2% APS plus 0.2% TEMED in ddH$_2$O for 2.5 h at 37°C with gentle agitation, followed by two washes in ddH$_2$O, each for 30 min at first 37°C then RT.

Stabilizing hydrogel: expanded hydrogels were next pre-incubated on ice-water for either 3.5 (mouse) or 4.5 h (human) with stabilizing hydrogel monomer solution (10% AA, 0.025% BIS, 0.05% TEMED, and 0.05% APS in ddH$_2$O; all w/v). After removing excess monomer solution, the hydrogel was sandwiched between a 22-mm square coverslip and an 18-mm round coverslip, and surrounded by monomer solution. Gelation was then carried out for 2 h at 37°C in a pre-warmed (37°C) humidified chamber. Gels were washed with ddH$_2$O for 30–60 min at RT. Unreacted crosslinker was neutralized by 0.2% APS and 0.2% TEMED in ddH$_2$O for 2.5 h at 37°C, followed by successive 30 min ddH$_2$O washes at 37°C and RT.

Second expandable hydrogel: samples were next pre-incubated on ice-water with the monomer solution for the second expandable hydrogel (19% SA, 10% AA, 0.025% BIS, 0.05% TEMED, and 0.05% APS in ddH$_2$O; all w/v) for 3.5 (mouse) or 4.5 h (human). The hydrogel was again sandwiched between a 22-mm square and a 18-mm round coverslip, surrounded by monomer solution, before gelation for 2 h at 37°C in a pre-warmed humidified chamber.

Protein labeling: pan-protein staining was performed with either 40 μM ATTO 488 NHS-ester or 40 μM AF488 NHS-ester in PBS overnight at 4°C while shaking. Hydrogels were expanded for around 4 h in regularly exchanged ddH$_2$O before imaging.

Images were acquired using an ANDOR Dragonfly spinning disk microscope with a 40x objective lens as described above. Samples were trimmed to the region of interest and mounted in ddH$_2$O on poly-L-lysine-coated 40 mm round coverslips (Bioptechs, Butler, PA, USA) in a custom-built aluminum chamber, stabilized by surrounding with two-component dental silicone (twinsil extrahart, picodent). CA3 primary dendrites were identified by their thorn-studded morphology, and both dendrite and large boutons encasing

thorny excrescences were 3D-segmented manually using VAST Lite (v1.4.0,[85]). Reconstructed dendritic length covered with thorns was measured in Neutube and used to determine the bouton density per unit length. 3D visualizations were created in VAST Lite. In human tissue specifically, multiple boutons contacting the dendrite of interest were observed to be connected by axon segments, thus arising from a common presynaptic cell (Figure S8). In these instances, boutons were not counted individually to best estimate the number of presynaptic cells. This complex arrangement may cause subtle overestimation of human input density, as further interconnectivity between counted boutons may occur through cable outside the imaged volume. The mean length of reconstructed thorny dendrite was 18 ± 2 μm and 48 ± 7 μm for mouse and human samples, respectively. Postmortem samples were analyzed similarly, using images acquired from both *stratum oriens* and *stratum radiatum* of CA3 of the 5 h postmortem sample. Dendrites with dendritic spines were reconstructed manually and as completely as possible within the imaged volumes (mean length of reconstructed dendrite was 18 ± 3 μm and 18 ± 2 μm per mouse and human segment, respectively).

Estimates of neuronal numbers

Estimates of neuronal numbers in rodents were used from the Hippocampome database and recent meta analyses.[30,93] Human neuronal densities used the mean values of separate stereology studies.[33–36] Neuronal counts are reported for combined CA3 and CA2 fields. The estimate of neuronal numbers in human CA3 alone were acquired by measurement of the relative CA3 and CA2 layer lengths in the hippocampal body from a detailed field parcellation study[32] to determine the scaling factor: CA3 ≈ 67% of CA3-2.

Mathematical modeling of CA3 function

Pattern completion analysis was performed in an autoassociative memory network model described in previous works.[14,50,51,94] The properties that define the model are: (1) usage of binary neurons (there is no subthreshold activity), (2) linear global inhibition (proportional to total network activity), (3) global threshold, (4) random initial recurrent excitatory connectivity, (5) clipped Hebbian plasticity, and (6) iterative recall. The network is initiated with a random connectivity matrix W_{ij} such that $P(W_{ij} = 1) = c_{ij}$, where c_{ij} is the connectivity probability between neurons i and j. The learning phase gives a Hebbian modification to W_{ij}, denoted J_{ij}, that accounts for simultaneous co-firing in any of the m memory patterns. Memory patterns ($\mathbf{Z}^p$, for p = 1,…, m) are sequences of 0s and 1s, which correspond to activation (1) or inactivation (0) of the excitatory neurons (n) during that memory. Thus, for i,j = 1,2,…, n: $J_{ij} = 1$ if $Z_i^p \cdot Z_j^p = 1$. The total connection strengths between the neurons are then described by $J_{ij} \cdot W_{ij}$.

To account for the differences between hippocampal sizes, we modeled the network using realistic sizes. Due to the large number of excitatory neurons of the human hippocampus (> 10^6) and the computational power it would require, instead of a simulation-based approach (such as in Guzman et al.[14]), an analytical approximation of the model was used.[51,94] The analytical approximation uses the central limit theorem over the above framework to provide a recursive set of coupled equations that describes the expected time evolution of neuronal activity in the system. Because the patterns are random, an arbitrary target pattern can be chosen to compute its recall without loss of generality. Furthermore, because neuron order is also random, this target pattern can be $\mathbf{Z}^0$, such that $Z_i^0 = 1$ for i = 1, …, n·a, and $Z_i^0 = 0$ for i = n·a+1, …, n. The first n·a neurons, also called valid neurons, will be the ones conforming this particular memory pattern and will be described by the variable x_t, while the other n·(1-a), also called spurious neurons, will be described by y_t.[94] The theoretical solution takes into account both spatial correlations between the learned connection strengths (i.e., correlations in J_{ij}) and temporal correlations between the state of the system and these connection strengths (i.e. correlations between J_{ij} and x_t, y_t), and can be used as an alternative solution that allows modeling human-size networks.

Variables and parameters[94]:

n	Total number of excitatory neurons	Parameter
$\bar{c}, \overline{c^2}$	Mean connectivity, and mean of the squared connectivity	Parameters
s, a	Ensemble size, and proportion of neurons belonging to the ensemble s / n	Parameters
m	Number of stored memories	Parameter
g_0	Global threshold of excitatory neurons	Parameter
g_1	Weight of the inhibitory neurons	Parameter
x_t	Average of the valid firing rate. $n \cdot a \cdot x_t$ is the expected number of valid firings at time t	Variable
y_t	Average of the spurious firing rate. $n \cdot (1-a) \cdot y_t$ is the expected number of spurious firings at time t	Variable
x_0	Initial condition for valid neurons, i.e., average valid firing at $t = 0$	Parameter
y_0	Initial condition for spurious neurons, i.e., average spurious firing at $t = 0$	Parameter
$E_i(t)$	Expectation of (*input – threshold*) for the *i*-th excitatory neuron at time t	Variable
$\sigma_i(t)$	Standard deviation of (*input – threshold*) for the *i*-th excitatory neuron at time t	Variable
μ_N, σ_N	Mean and standard deviation of the change in membrane potential due to synaptic input at a neuron	Parameters
ρ	Expectation of J_{ij}	Variable

(Continued on next page)

Continued

ρ′	Expectation of J_{ij} conditional on another J_{ij}	Variable
γ	Covariance of J_{ij} s	Variable
γ′	Covariance of J_{ij} s conditional on other J_{ij} s	Variable
r_t	Recall at time t, measured as the overlap between the state of the system and the memory to be recalled	Variable

A network will be defined by the parameters $n, \overline{c}, \overline{c^2}, s, m, g_0, g_1, \mu_N$, and σ_N, which are the parameters that have been explored in this work. Given that recurrent connectivity in CA3 lacks spatial dependence (this paper, and Guzman et al.[14]), we set $\overline{c^2} = (\overline{c})^2$.

The state of the system is described by a set of coupled equations that, when applied iteratively, reproduce the expected average firing rate values of the valid and spurious neurons over time.[51,94] These equations are:

$$x_{t+1} = \Phi(E_1(t) / \sigma_1(t)) \tag{Equation 1A}$$

$$y_{t+1} = \Phi(E_n(t) / \sigma_n(t)) \tag{Equation 1B}$$

$$x'_{t+1} = \Phi(E'_1(t) / \sigma'_1(t)) \tag{Equation 1C}$$

$$y'_{t+1} = \Phi(E'_n(t) / \sigma'_n(t)) \tag{Equation 1D}$$

where $\Phi(k)$ denotes the normal cumulative distribution at k, and:

$$E_1(t) = E(excitation) - E(inhibition) - g_0 \tag{Equation 2}$$

$$E_1(t) = \overline{c}\left(ax_t + (1-a)\rho y'_t\right) - g_1(ax_t + (1-a)y_t) - g_0 \tag{Equation 2A}$$

$$E_n(t) = \overline{c}\,\rho\left(ax'_t + (1-a)y'_t\right) - g_1(ax_t + (1-a)y_t) - g_0 \tag{Equation 2B}$$

$$E'_1(t) = \overline{c}\left(ax_t + (1-a)\rho' y'_t\right) - g_1(ax_t + (1-a)y_t) - g_0 \tag{Equation 2C}$$

$$E'_n(t) = \overline{c}\,\rho'\left(ax'_t + (1-a)y'_t\right) - g_1(ax_t + (1-a)y_t) - g_0 \tag{Equation 2D}$$

$$[n\sigma_1(t)]^2 = na(\overline{c} - \overline{c^2})x_t + n(1-a)\rho y'_t\left(\overline{c} - \overline{c^2}\,\rho\,\frac{y'_t}{y_t+\epsilon}\right) + n^2(1-a)^2\overline{c}^2\gamma y'^2_t \tag{Equation 3A}$$

$$[n\sigma_n(t)]^2 = na\rho x'_t\left(\overline{c} - \overline{c^2}\,\rho\,\frac{x'_t}{x_t+\epsilon}\right) + n(1-a)\rho y'_t\left(\overline{c} - \overline{c^2}\,\rho\,\frac{y'_t}{y_t+\epsilon}\right) + n^2\gamma\left(ax'_t+(1-a)y'_t\right)^2\overline{c}^2 \tag{Equation 3B}$$

$$[n\sigma'_1(t)]^2 = na(\overline{c} - \overline{c^2})x_t + n(1-a)\rho' y'_t\left(\overline{c} - \overline{c^2}\,\rho'\,\frac{y'_t}{y_t+\epsilon}\right) + n^2(1-a)^2\overline{c}^2\gamma' y'^2_t \tag{Equation 3C}$$

$$[n\sigma'_n(t)]^2 = na\rho' x'_t\left(\overline{c} - \overline{c^2}\,\rho'\,\frac{x'_t}{x_t+\epsilon}\right) + n(1-a)\rho' y'_t \cdot \left(\overline{c} - \overline{c^2}\,\rho'\,\frac{y'_t}{y_t+\epsilon}\right) + n^2\gamma'\left(ax'_t+(1-a)y'_t\right)^2\overline{c}^2 \tag{Equation 3D}$$

where the variables due to the correlations and covariances are defined as:

$$\rho = 1 - \left(1 - a^2\right)^m \qquad \text{(Equation 4A)}$$

$$\rho' = \frac{1 - 2\left(1 - a^2\right)^m + \left(1 - 2a^2 + a^3\right)^m}{\rho + \epsilon} \qquad \text{(Equation 4B)}$$

$$\gamma = \left(1 - 2a^2 + a^3\right)^m - \left(1 - a^2\right)^{2m} \qquad \text{(Equation 4C)}$$

$$\gamma' = \frac{1 - 3\left(1 - a^2\right)^m + 3\left(1 - 2a^2 + a^3\right)^m - \left(1 - 3a^2 + 3a^3 - a^4\right)^m}{\rho + \epsilon} - \rho'^2 \qquad \text{(Equation 4D)}$$

The progressive recall of the memory $\mathbf{Z}^0$ of a network at each time step t can be computed from the values of x_t and y_t with:

$$r_t = \frac{n_v - a(n_v + n_s)}{\sqrt{(n_v + n_s) \cdot \left(1 - \frac{(n_v + n_s)}{n}\right)} \cdot \sqrt{na(1 - a)}} \qquad \text{(Equation 5)}$$

where $n_v(t) = nax_t$ denotes the number of activated valid neurons at time t, and $n_s(t) = n(1 - a)y_t$ the number of activated spurious neurons.

To account for numerical errors, the value ϵ was set to 10^{-100}, and additional constraints were applied to variance and correlation coefficient during recall such that $(n \cdot \sigma)^2 \geq 0$ (Equations 3A–3D) and $r \geq 0$ (Equation 5). Changes in ϵ had only minimal effects on the results.

Synaptic variability: to incorporate the effect of quantal release, the previous equations were expanded to include the mean and standard deviation unitary EPSP amplitudes, μ_N and σ_N[51,94]:

$$x_{t+1}^q = \Phi\left(E_1^q(t) \,/\, \sigma_1^q(t)\right) \qquad \text{(Equation 6A)}$$

$$y_{t+1}^q = \Phi\left(E_n^q(t) \,/\, \sigma_n^q(t)\right) \qquad \text{(Equation 6B)}$$

$$x_{t+1}'^q = \Phi\left(E_1'^q(t) \,/\, \sigma_1'^q(t)\right) \qquad \text{(Equation 6C)}$$

$$y_{t+1}'^q = \Phi\left(E_n'^q(t) \,/\, \sigma_n'^q(t)\right) \qquad \text{(Equation 6D)}$$

where:

$$E_1^q(t) = \overline{c}\left(ax_t + (1 - a)\rho y_t'\right)\mu_N - g_1(ax_t + (1 - a)y_t) - g_0 \qquad \text{(Equation 7A)}$$

$$E_n^q(t) = \overline{c}\,\rho\left(ax_t' + (1 - a)y_t'\right)\mu_N - g_1(ax_t + (1 - a)y_t) - g_0 \qquad \text{(Equation 7B)}$$

$$E_1'^q(t) = \overline{c}\left(ax_t + (1 - a)\rho'y_t'\right)\mu_N - g_1(ax_t + (1 - a)y_t) - g_0 \qquad \text{(Equation 7C)}$$

$$E_n'^q(t) = \overline{c}\,\rho'\left(ax_t' + (1 - a)y_t'\right)\mu_N - g_1(ax_t + (1 - a)y_t) - g_0 \qquad \text{(Equation 7D)}$$

$$\left[n\sigma_1^q(t)\right]^2 = n\sigma_N^2\,\overline{c}\left(ax_t + (1 - a)\rho y_t'\right) + \mu_N^2[n\sigma_1(t)]^2 \qquad \text{(Equation 8A)}$$

$$\left[n\sigma_n^q(t)\right]^2 \;=\; n\sigma_N^2\,\overline{c}\,\rho\left(ax_t + (1-a)y_t'\right) + \mu_N^2\left[n\sigma_n(t)\right]^2 \qquad \text{(Equation 8B)}$$

$$\left[n\sigma_1^{'q}(t)\right]^2 = n\sigma_N^2\,\overline{c}\,\left(ax_t + (1-a)\rho' y_t'\right) + \mu_N^2\left[n\sigma_1(t)\right]^2 \qquad \text{(Equation 8C)}$$

$$\left[n\sigma_n^{'q}(t)\right]^2 = n\sigma_N^2\,\overline{c}\,\rho'\left(ax_t + (1-a)y_t'\right) + \mu_N^2\left[n\sigma_n(t)\right]^2 \qquad \text{(Equation 8D)}$$

For the special case of $\mu_N = 1$ and $\sigma_N = 0$, these equations (Equations 6, 7, and 8) are equivalent to the previous ones (Equations 1, 2, and 3).

To compute the maximum number of patterns that the network is able to reliably store and retrieve, we initialized the network with the target memory $\mathbf{Z}^0$, by defining $x_0 = 1$, $y_0 = 0$, and computed the evolution of the system by iterating the progressive recall equations until no further change occurred. If the network is able to successfully sustain the initial state (high r_{final}), it can store that many number of memories m. However, if this final stable state has low overlap with $\mathbf{Z}^0$ (low r_{final}), the network was not able to properly learn the m memories.[51] This process is repeated for several total values of stored memories m and g_1. The number of maximum storable memories (M) is defined as the maximum m that gives a $r_{final} > r_{min}$ for any g_1, with $r_{min} = 0.6$. A maximum number of iterations was set to 50. Conclusions remain the same for $x_0 < 1$.

To make the comparison between network sizes consistent with basic biological properties of the hippocampus, we fixed the total number of synapses of the network, and distributed them in small highly connected networks (small n, high c), or increasingly bigger and less connected networks (high n, small c). Total number of synapses was fixed to 2, 4, 8, 16, 32, and $60 \cdot 10^9$. Tested connectivity ranged from 0.0003 to 0.2, divided in 69 non-linearly spaced intervals. For each connectivity value, the corresponding number of neurons was computed for all total number of synapses using $n = \sqrt{\frac{\#\ synapses}{c}}$.

SBI is an approach for estimating the probability density (or likelihood) $p(z|\{params\})$ of a set of parameters $\{params\}$ for a given observation z in models for which the likelihood is analytically intractable but simulations are possible.[52] Such intractability is present for many models in neuroscience, so SBI has been shown to be a successful approach for performing Bayesian inference in computational neuroscience.[53,95] SBI can infer the model parameters most likely to have generated z (i.e., the posterior distribution $p(\{params\}|z)$), using samples from a prior distribution $\{params\} \sim P(\{params\})$ and their corresponding model output $z \sim p(z|\{params\})$, by applying Bayes' rule such that $p(\{params\}|z) \propto p(z|\{params\}) \cdot P(\{params\})$. In this work, we followed the algorithms proposed by Gonçalves et al.,[53] in which this is achieved by training an artificial neural network to map any simulation result onto a range of possible parameters.

To apply this algorithm to our CA3 model, we explored the most relevant parameters of the models, which are the connection probability c, ensemble size s, quantal variability σ_N, threshold g_0, and inhibitory weight g_1 (because of lack of experimental information). The remaining parameters were fixed to $x_0 = 1$, $y_0 = 0$, and $\mu_N = 1$ (making $CV = \sigma_N/\mu_N = \sigma_N$). In addition, we fixed the total number of synapses to either $2 \cdot 10^9$ (mouse hippocampal CA3) or $60 \cdot 10^9$ (human hippocampal CA3), and performed SBI analysis independently for both sizes. The number of neurons was again computed as a function of connection probability and number of synapses.

Prior distributions for the free parameters were: $c \in [10^{-3}, 10^{-1}]$, $g_0 \in [10^{-8}, 10^{-6}]$, $g_1 \in [10^{-3}, 10^{-1}]$, $s \in [10^2, 10^3]$, and $\sigma_N \in [0, 1]$. All c, g_0, g_1, and s were mapped in a logarithmic manner, so the priors were set to be [-3, -1], [-8, -6], [-3, -1], and [2, 3], respectively, and the chosen value was transformed to the power of 10. SBI was trained with 100,000 simulations (each for mouse and human hippocampus sizes), using the 'SNPE' method and 8 'workers'.[86] Posterior distributions were computed by setting the observation to a specific target m, and sampling from the trained network 10,000 times.

Model implementation was run on a Lenovo ThinkPad L14 Gen 4 with 16 GB of memory, a 13th Gen Intel® Core™ i5-1335U × 12 processor and Mesa Intel® Graphics (RPL-P), over Ubuntu 22.04.3 LTS. Python 3.7.12 and numpy 1.21 were used for all numerical operations, and scipy 1.11 for the normal cumulative distribution. For SBI implementation, torch 1.13 and sbi 0.22 were also used.

QUANTIFICATION AND STATISTICAL ANALYSIS

All data are reported as mean ± SEM throughout text and legends, or median with interquartile range where specified. Box plots depict data as median (line), 25th and 75th quartile (box), and min/max points (whiskers). Symbols with errors depict mean ± SEM. Proportional datasets were compared using Fisher's exact test (e.g. for connectivity) for either two or three conditions. Pairwise comparisons were made using individual Fisher's exact tests with Benjamini-Hochberg correction for multiple comparisons. As biological datasets rarely exhibit a normal distribution, non-parametric statistical tests for either two-sample (Mann-Whitney test) or multi-sample (Kruskal-Wallis test with Dunn's multiple comparisons test) data were applied as appropriate, unless specified otherwise. Where Kruskal-Wallis tests were applied, the pairwise p values presented on figures depicted the result of Dunn's multiple comparisons test. Statistical tests were performed using GraphPad Prism 9 or 10, and exact p values were reported throughout the manuscript. Values and units of n are provided in figure legends throughout the paper.
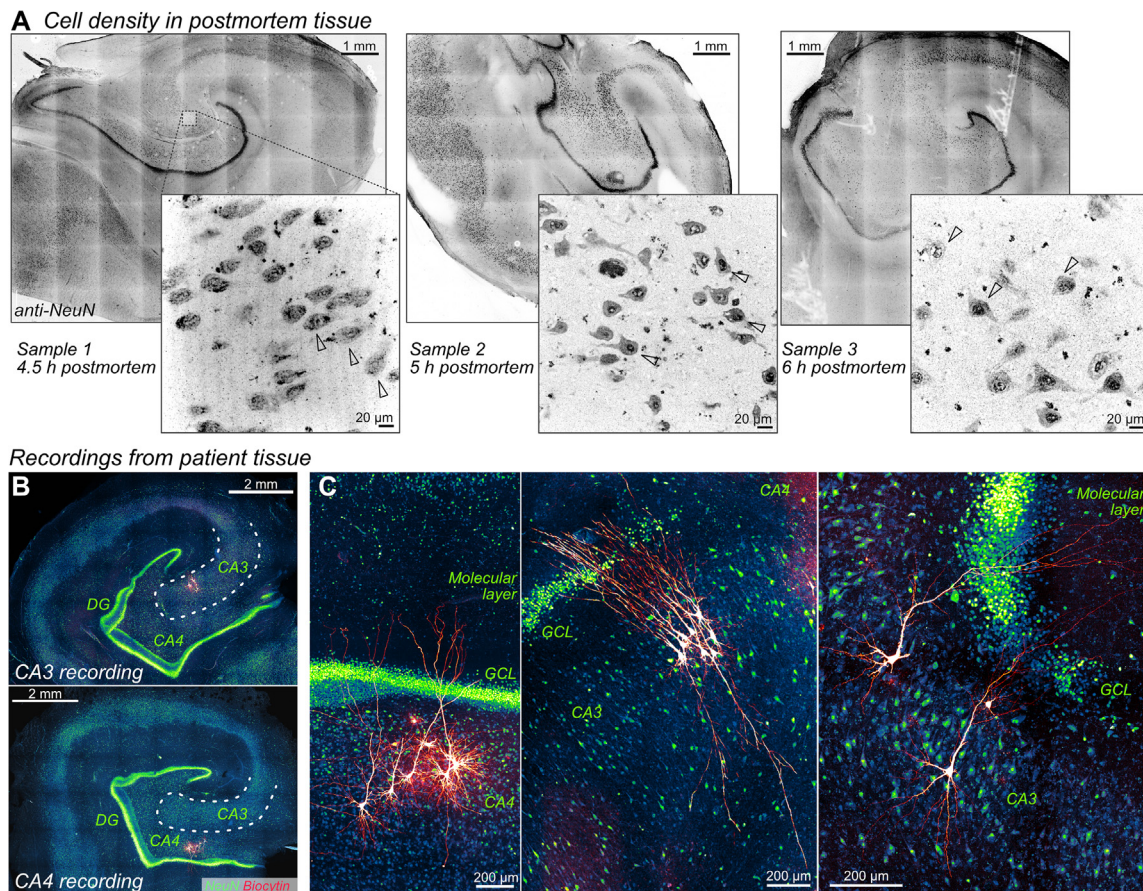
Supplemental figures

A *Cell density in postmortem tissue*

anti-NeuN

Sample 1
4.5 h postmortem

Sample 2
5 h postmortem

Sample 3
6 h postmortem

Recordings from patient tissue

B
CA3 recording
CA4 recording

C

Figure S1. Anatomical features of human hippocampus, related to Figure 1

(A) Example images of NeuN-stained hippocampal slices from postmortem donors with no known neurological deficits. Insets demonstrate cell density in the CA3 pyramidal cell layer, with neurons indicated (arrowheads).

(B) Multicellular recording examples from CA3 (upper) and CA4 (lower) of the human hippocampus, with CA3 defined as cells within the structured neuronal layer (white dashed lines) extending out from between the dentate gyrus granule cell layers (DG GCL).

(C) Examples of recorded human CA3/4 PNs showing apical dendrite crossing of the DG GCL (red, intracellular biocytin; blue-green, anti-NeuN).
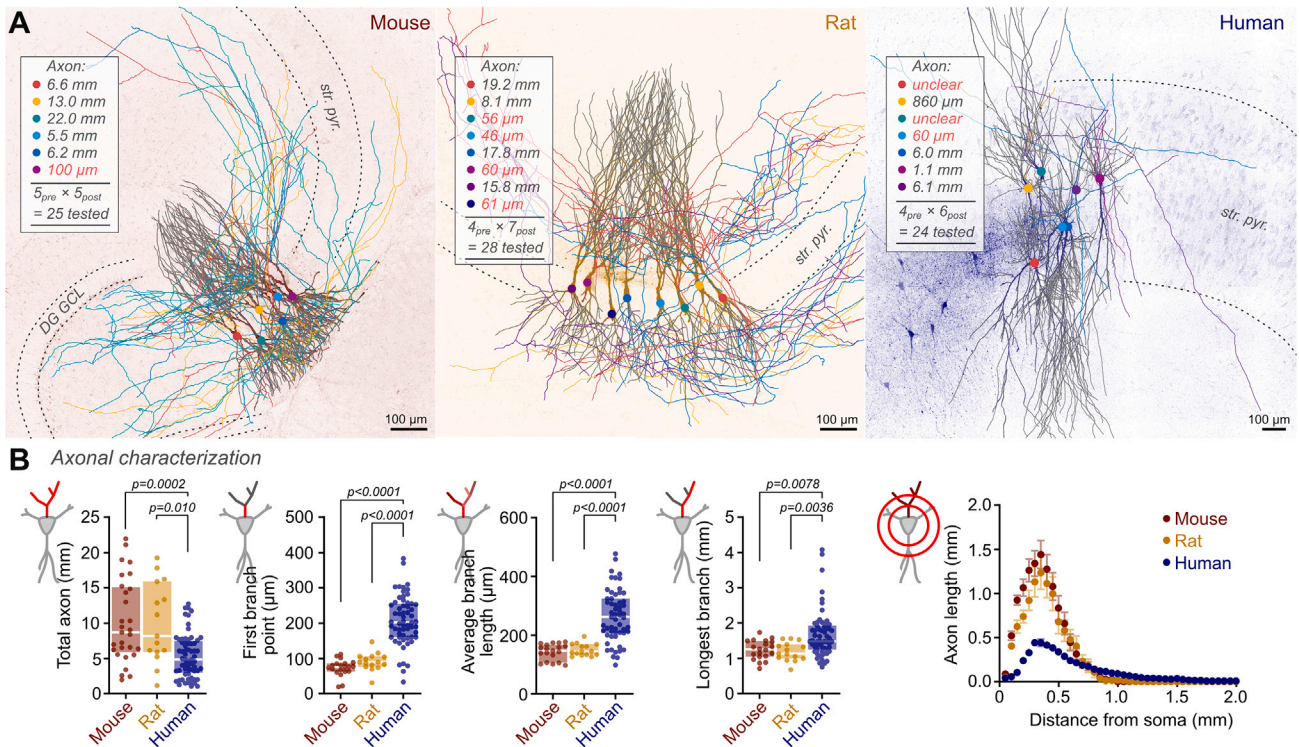
Figure S2. CA3 PN axonal branch properties across species, related to Figure 2

(A) Example multicellular recordings across species to demonstrate axonal cutting analysis. Cells with greater than 0.5 mm of reconstructable axon were included in the "corrected" connectivity analysis, which excluded cells with axons exiting the slice before extensive collateralization, or without visible axons. These criteria will limit slicing-induced underestimation of intercellular connectivity. Maximum intensity projections of streptavidin-AF647-visualized recorded neurons are overlaid with reconstructed morphologies. Dendrites are depicted in gray, while individual cell axons/somata are colored, with quantified length inset. DG GCL and CA3 *stratum pyramidale* (str. pyr.) are delineated.

(B) The length of reconstructable axon per neuron is greater in rodent than in human tissue slices (line, box, and whiskers depict median, 25th–75th percentiles, and min/max values; mean ± SEM; mouse, 10.2 ± 1.1 mm, $n = 29$; rat, 10.0 ± 1.5 mm, $n = 15$; human, 5.40 ± 0.4 mm, $n = 65$; Kruskal-Wallis test, $p < 0.0001$). The reduction in axon length for human CA3 cells results from their less frequent collateralization. Axonal length to the first branch point is substantially greater in human than rodent CA3 PNs (mouse, 73 ± 5 μm, $n = 20$; rat, 90 ± 7 μm, $n = 15$; human, 208 ± 9 μm, $n = 60$; Kruskal-Wallis test, $p < 0.0001$), and the average axonal length between branch points is also greater in humans than rodents (mouse, 143 ± 6 μm, $n = 19$; rat, 150 ± 5 μm, $n = 15$; human, 266 ± 12 μm, $n = 57$; Kruskal-Wallis test, $p < 0.0001$). Despite this, the longest axonal branch reconstructable was greatest in human neurons, reflecting the greater size of tissue slice and axonal extent (mouse, 1.24 ± 0.06 mm, $n = 20$; rat, 1.19 ± 0.07 mm, $n = 15$; human, 1.68 ± 0.08 mm, $n = 62$; Kruskal-Wallis test, $p = 0.0003$). Axonal Sholl analysis demonstrates the reduced axonal extent in human tissue, with a shifted distribution indicative of a broader axonal arborization (mean ± SEM presented). Only cells with > 0.5 mm reconstructable axon were included in (B) and are a subset of recorded cells that are fully reconstructed.
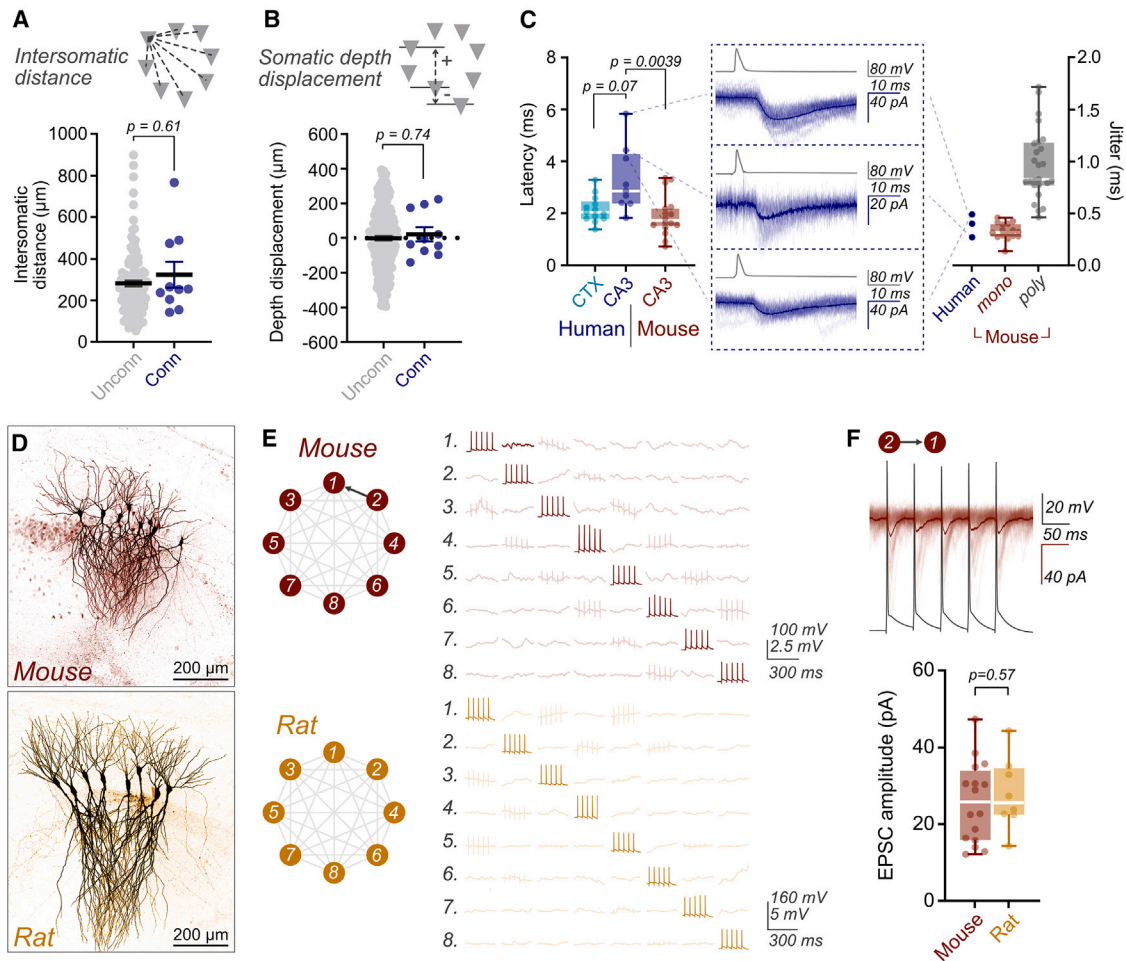
Figure S3. Measuring human and rodent CA3 synaptic properties, related to Figure 2

(A) No distance dependence to human CA3 connectivity was observed. Intersomatic distance (3D Euclidean distance between somatic centers) was similar between unconnected and synaptically connected CA3 neurons (mean ± SEM presented; unconnected, 281 ± 15 μm, $n = 111$; connected, 324 ± 62 μm, $n = 10$; Mann-Whitney test, $p = 0.61$).

(B) No preferential directionality was observed for human CA3 connections on the deep-superficial axis. Difference in somatic depth within *stratum pyramidale* for recorded cell pairs is plotted, with positive values representing connections in the direction of *stratum oriens* (mean ± SEM presented; unconnected, −1 ± 12 μm, $n = 232$; connected, 22 ± 41 μm, $n = 10$; Mann-Whitney test, $p = 0.74$).

(C) Latency of human CA3 connections is longer than recorded in mouse CA3 (line, box, and whiskers depict median, 25th–75th percentiles, and min/max values; human cortex, 2.2 ± 0.1 ms, $n = 13$; human CA3, 3.3 ± 0.4 ms, $n = 9$; mouse CA3, 1.9 ± 0.2 ms, $n = 16$; Kruskal-Wallis test, $p = 0.0054$). Long latency (> 4 ms) human CA3 connections are likely to be monosynaptic, due to their reliability and low jitter (right). Jitter values (SD of latency) are in line with mouse putative monosynaptic connections and much lower than mouse putative polysynaptic connections (jitter: mouse monosynaptic, 0.32 ± 0.02 ms, $n = 16$; mouse polysynaptic, 0.97 ± 0.07 ms, $n = 25$).

(D) Example images of octuple patch-clamp-recorded CA3 cells from mouse (upper) and rat (lower).

(E) Example recordings from mouse and rat CA3 PNs. Each recorded neuron is depicted as a row (labeled) of the recording array. Averaged voltage traces in response to presynaptic cell spiking (diagonal) are shown in bold, with, and faded, without, identified monosynaptic connections. Connectivity schemes for these recordings are depicted (left).

(F) Voltage-clamp recording of synapse identified in (E). Individual sweeps (faded) are overlaid with the average trace, with presynaptic cell spiking depicted (gray). Peak amplitudes of unitary EPSCs are similar between mouse and rat connections (mouse, 25.8 ± 2.6 pA, $n = 16$; rat, 27.9 ± 3.3 pA, $n = 8$; Mann-Whitney test, $p = 0.57$).
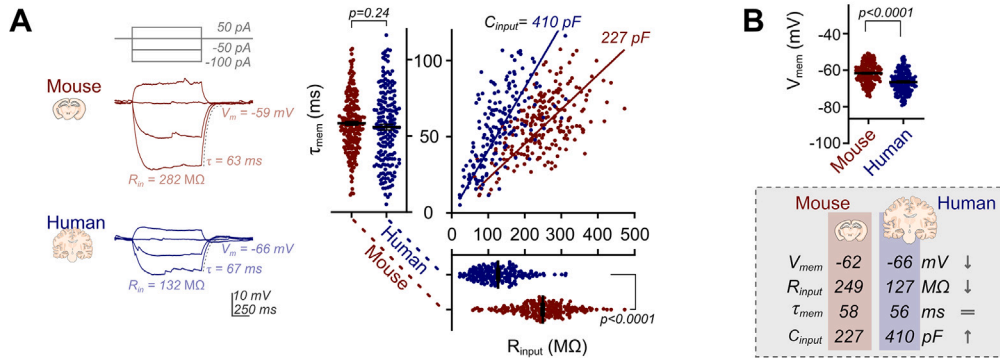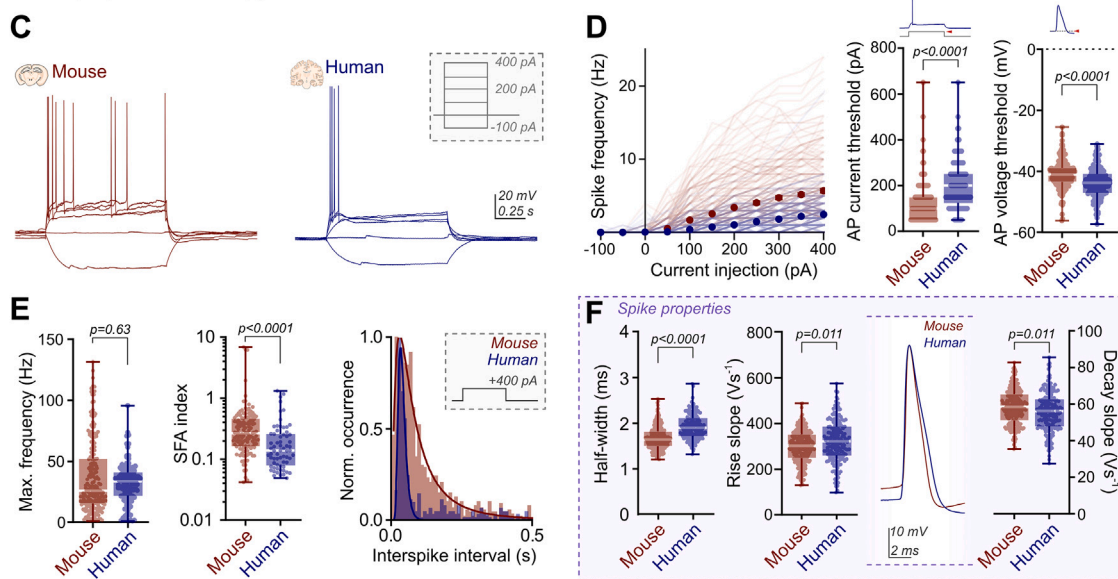
Figure S4. CA3 PN passive and active membrane properties across species, related to Figure 3

(A) Human CA3 PNs have lower input resistance (lines and error bars depict mean ± SEM; mouse, 249 ± 5 MΩ, n = 232; human, 127 ± 4 MΩ, n = 187; Mann-Whitney test, $p < 0.0001$) but similar membrane time constant (mouse, 58.3 ± 1.2 ms, n = 229; human, 55.9 ± 1.8 ms, n = 185; Mann-Whitney test, p = 0.24) to mouse CA3 PNs, which correspond to an increased cell capacitance (linear fit of input resistance vs. membrane time constant scatter, human: 410 pF, mouse 227 pF).

(B) The resting membrane potential of human CA3 PNs is subtly more negative than that of mice (mouse, −61.8 ± 0.4 mV, n = 232; human, −66.5 ± 0.4 mV, n = 187; Mann-Whitney test, $p < 0.0001$).

(C) Example traces of mouse and human AP responses to current injection (inset).

(D) Mouse neurons give greater spiking (across 1-s stimulus; symbols, mean ± SEM; lines, individual cells), with lower current threshold for spike generation (line, box, and whiskers depict median, 25th–75th percentiles, and min/max values; rheobase, minimum current for spiking: mouse, 126 ± 5 pA, n = 232 cells; human, 200 ± 8 pA, n = 185 cells; Mann-Whitney test, $p < 0.0001$). AP threshold is subtly lower in human PNs (mouse, −40.9 ± 0.3 mV, n = 232; human, −43.6 ± 0.4 mV, n = 184; Mann-Whitney test, $p < 0.0001$).

(E) CA3 neurons exhibit maximal spiking at current onset, which is more pronounced in human neurons, as observed through multiple parameters. Maximum firing rate at 400 pA injection has similar mean values between species (mouse, 37 ± 2 Hz, n = 212; human, 32 ± 1 Hz, n = 120; Mann-Whitney test, p = 0.63), however with heterogeneous distributions. The majority of mouse neurons fire at lower frequency than human neurons. Spike-frequency adaptation (SFA) is markedly stronger in human neurons, giving a lower SFA index (mouse, 0.47 ± 0.08, n = 128; human, 0.23 ± 0.03, n = 66; Mann-Whitney test, $p < 0.0001$). The distribution of interspike intervals across all cells (400 pA injection) is much narrower for human neurons, demonstrating more precise spike timing.

(F) The half-width of human spikes is subtly longer than those of mice (mouse, 1.68 ± 0.02 ms, n = 232; human, 1.93 ± 0.02 ms, n = 184; Mann-Whitney test, $p < 0.0001$), with slower maximal decay slope (mouse, 58.6 ± 0.6 V s^{-1}, n = 232; human, 55.8 ± 0.8 V s^{-1}, n = 184; Mann-Whitney test, p = 0.011) and faster rise slope (mouse, 298 ± 5 V s^{-1}, n = 231; human, 322 ± 7 V s^{-1}, n = 184; Mann-Whitney test, p = 0.011).
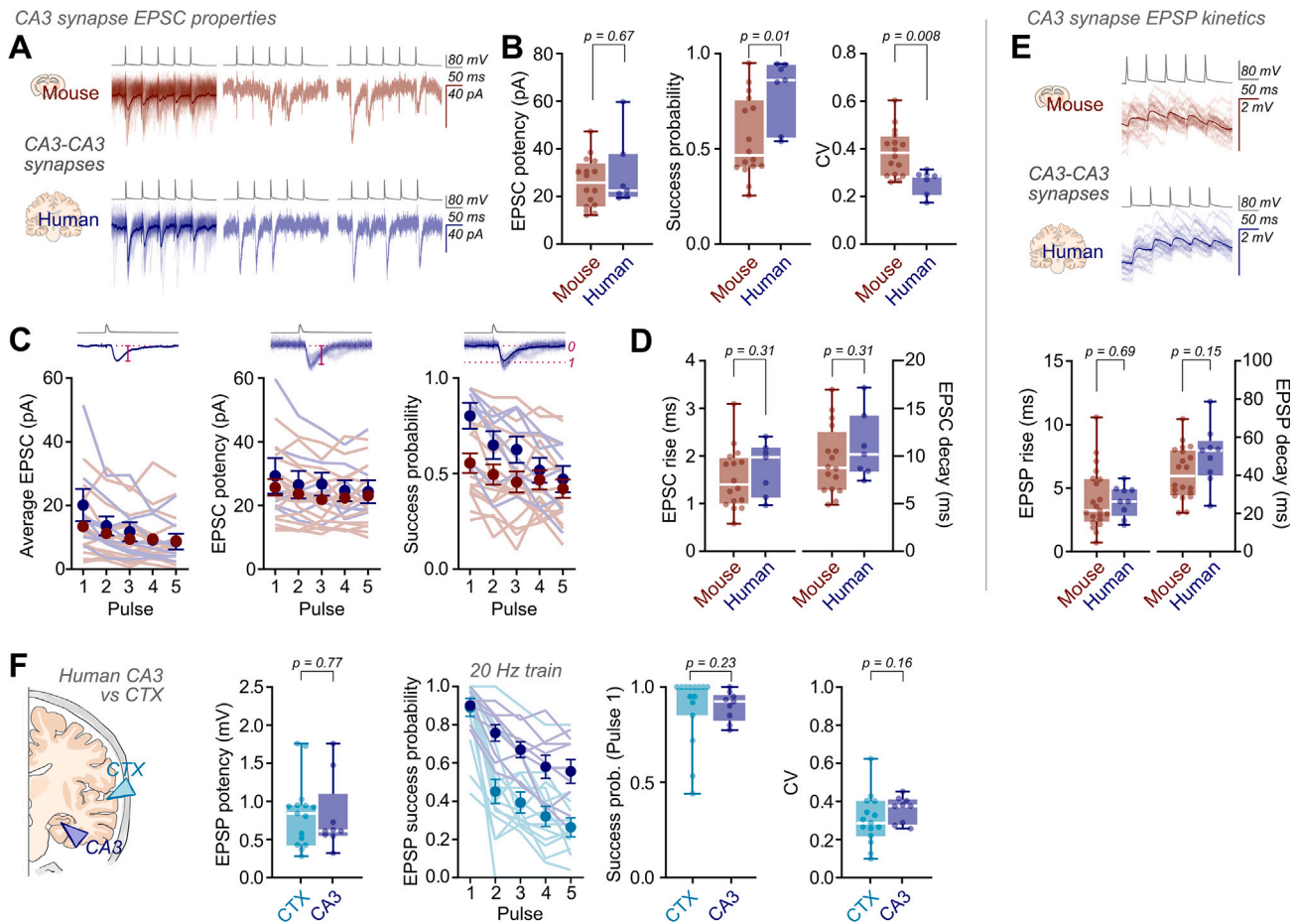
Figure S5. Increased synaptic reliability in the human brain, related to Figure 3

(A) Example traces of unitary EPSCs from mouse (upper) and human (lower) CA3 PN pairs. Average traces (bold) are depicted over individual traces (left), with example sweeps presented (right).

(B) Average EPSC potency was unchanged between species (line, box, and whiskers depict median, 25th–75th percentiles, and min/max values; mouse, 25.8 ± 2.6 pA, $n = 16$; human, 29.4 ± 5.6 pA, $n = 7$; Mann-Whitney test, $p = 0.67$), while success probability was significantly higher (mouse, 0.56 ± 0.05, $n = 16$; human, 0.80 ± 0.07, $n = 7$; Mann-Whitney test, $p = 0.010$) and CV of success amplitudes significantly lower in human synapses (mouse, 0.39 ± 0.02, $n = 16$; human, 0.26 ± 0.02, $n = 7$; Mann-Whitney test, $p = 0.008$).

(C) Individual (lines) and average (circles; mean ± SEM) responses to 20-Hz train stimulation. Average EPSCs (left), are produced from EPSCs of a similar potency throughout trains and between species (center), with different success probabilities (right).

(D) EPSC kinetics appeared unchanged between mouse and human CA3 synapses (EPSC 20%–80% rise time: mouse, 1.54 ± 0.16 ms, $n = 16$; human, 1.74 ± 0.21 ms, $n = 7$; Mann-Whitney test, $p = 0.31$; EPSC decay time constant: mouse, 9.55 ± 0.90 ms, $n = 16$; human, 11.02 ± 1.33 ms, $n = 7$; Mann-Whitney test, $p = 0.31$).

(E) EPSPs (20-Hz train stimulation traces) of unitary CA3 synapses have similar kinetics between mice and humans (EPSP 20%–80% rise time: mouse, 4.1 ± 0.5 ms, $n = 21$; human, 4.0 ± 0.4 ms, $n = 9$; Mann-Whitney test, $p = 0.69$; EPSP decay time constant: mouse, 41.1 ± 3.1 ms, $n = 20$; human, 50.6 ± 5.1 ms, $n = 9$; Mann-Whitney test, $p = 0.15$).

(F) Human CA3 and neocortical synapses showed not only similar potency (CTX, 0.84 ± 0.11 mV, $n = 15$; CA3, 0.80 ± 0.16 mV, $n = 9$; Mann-Whitney test, $p = 0.77$) but also similarly high success probability for the first pulse of 20-Hz trains (CTX, 0.89 ± 0.05, $n = 15$; CA3, 0.90 ± 0.03, $n = 9$; Mann-Whitney test, $p = 0.23$) and similarly low CV (CTX, 0.30 ± 0.03, $n = 15$; CA3, 0.36 ± 0.02, $n = 9$; Mann-Whitney test, $p = 0.16$), suggesting that synaptic reliability is a general feature of the human brain.
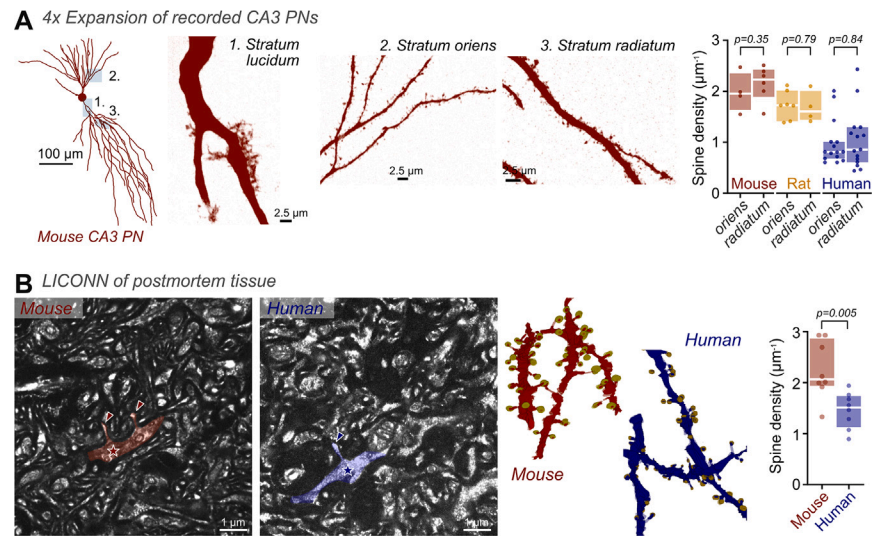
A *4x Expansion of recorded CA3 PNs*

Mouse CA3 PN

1. *Stratum lucidum*

2. *Stratum oriens*

3. *Stratum radiatum*

B *LICONN of postmortem tissue*

Mouse *Human*

Human

Mouse

Figure S6. Spine density comparison across layers and species, related to Figure 4

(A) Reconstructed mouse neuron (left, skeleton), with labeled areas imaged by 4× expansion microscopy (center). Image scale bars depict pre-expansion sizes. Measured spine density (per μm dendrite length) shows no difference between dendrites in *stratum oriens* or *radiatum* across species (line, box, and whiskers depict median, 25th–75th percentiles, and min/max values; mean ± SEM; mouse: *stratum oriens*, 1.98 ± 0.19 μm^{-1}, $n = 4$; *stratum radiatum*, 2.16 ± 0.14 μm^{-1}, $n = 6$; Mann-Whitney test, $p = 0.35$; rat: *stratum oriens*, 1.73 ± 0.10 μm^{-1}, $n = 7$; *stratum radiatum*, 1.68 ± 0.15 μm^{-1}, $n = 4$; Mann-Whitney test, $p = 0.79$; human: *stratum oriens*, 0.98 ± 0.11 μm^{-1}, $n = 15$; *stratum radiatum*, 1.04 ± 0.15 μm^{-1}, $n = 15$; Mann-Whitney test, $p = 0.84$).

(B) Example LICONN images of CA3 from fresh frozen postmortem mouse and human tissue. Example spiny dendrites (marked with stars) and spines (marked with arrowheads) are highlighted. 3D dendrite reconstructions are presented with spine heads marked yellow (mouse, red; human, blue). Spine density was lower in human than mouse CA3 in these non-epileptic samples, confirming reduced input density in human CA3 (mouse, 2.24 ± 0.20 μm^{-1}, $n = 8$ segments; human, 1.45 ± 0.13 μm^{-1}, $n = 8$ segments; Mann-Whitney test, $p = 0.005$; data from 1 human donor, 5 h postmortem interval).
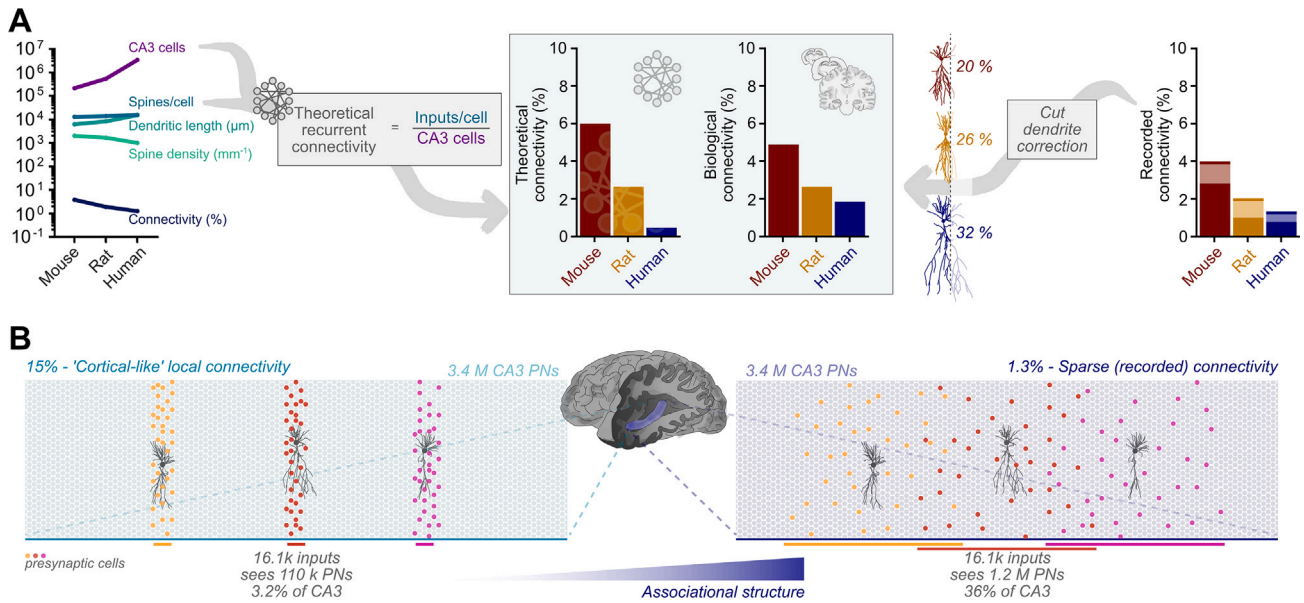
Figure S7. Theoretical analysis of recurrent collateral synapses predicts sparse connectivity, related to Figure 4

(A) Theoretical connectivity values for a broad recurrent network can be calculated anatomically from the number of network nodes (CA3 neurons) and inputs per node (spines/cell), which predicts mouse, rat, and human CA3 connectivity at 5.99%, 2.65%, and 0.47%, respectively. These values are comparable to the estimated connectivity from recordings, indicating that CA3 approximates a broad recurrent network across species. Connectivity after correction for both axon cutting (as previous) and percentage of recorded cell dendrites lost by slicing gives "biological connectivities": mouse, 4.89%; rat, 2.65%; human, 1.86%.

(B) Sparse CA3 connectivity forms a broad associational network. Dense, neocortical levels of local connectivity (left) would imply that individual CA3 PNs receive all 16,100 inputs from just 3.2% of the total CA3 volume. Sparse local connectivity, as recorded (right), allows for broader, long-range influence on individual CA3 PNs, forming a broad associational network. Colors represent putative presynaptic cells to each CA3 PN, constrained by dense or sparse connectivity. Human brain schematic depicting hippocampus (blue), based on Gray's Anatomy of the Human Body.[96]
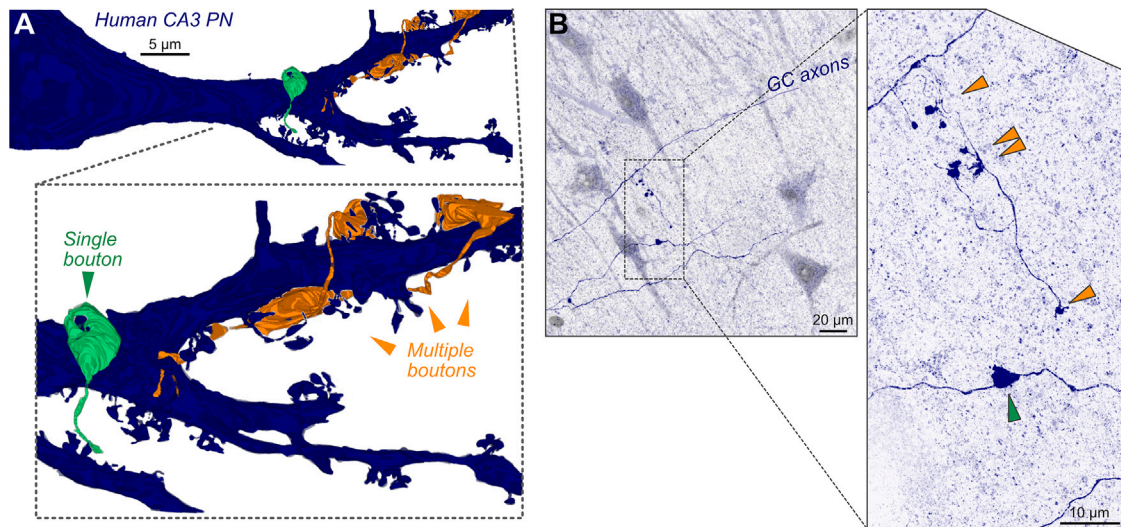
Figure S8. Multi-bouton contacts in the human mossy-fiber-to-CA3 pathway, related to Figure 6

(A) Examples of both single (green) and multiple (orange) boutons from individual GC axons contacting a single human CA3 PN (blue), reconstructed from LICONN data from patient 10 (see Figure 6 for main dataset).

(B) Incidentally biocytin-labeled human GC axons also demonstrate both classical "single-bouton" and "multi-bouton" output sites (images from patient 10). Biocytin-stained GC axons (blue) crossing the CA3 subfield in human slices stained with NeuN (gray) are presented using confocal imaging (left) and 4× expansion microscopy (right, inset). Examples of an individual large bouton (green) and multiple "beads-on-a-string" boutons (orange) are indicated with arrowheads. Scale bars represent pre-expansion sizes in all cases.